Atmospheric correction and inherent optical property estimation in the southwest New Caledonia lagoon using AVNIR-2 high-resolution data

Hiroshi Murakami, Cecile Dupouy

Atmospheric correction and inherent optical property estimation in the southwest New Caledonia lagoon using AVNIR-2 high-resolution data

Hiroshi Murakami[1,*], Cécile Dupouy[2]

[1] *Japan Aerospace Exploration Agency, Earth Observation Research Center, 2-1-1, Sengen, Tsukuba, Ibaraki, Japan 305-8505*

[2] *Aix-Marseille University, University of South Toulon Var, CNRS/INSU, IRD, MIO, UM 110 Centre IRD of Noumea, BP A5, 98848, Noumea, New Caledonia*

**Corresponding author: murakami.hiroshi.eo@jaxa.jp*

Abstract

Retrievals of inherent optical properties (IOPs) and Chlorophyll-a concentration (*Chla*) was investigated for AVNIR-2 images with 30-m spatial resolution and four bands in the southwest tropical lagoon of New Caledonia. We corrected the atmospheric and sea-surface reflectance iteratively through the retrieval of IOPs. After an additional correction of sea floor reflectance, the estimated IOPs and *Chla* agreed well with the in situ measurements even in the lagoon areas. This study provides a method to allowing a local optimal estimation of IOPs and *Chla* with a high resolution sensor by preparation of the candidate spectra for the target areas.

1. INTRODUCTION

1.1 Ocean color retrievals in the coastal areas

Ocean color retrieval is a challenge in the coastal areas but is a powerful tool for coastal surveys. Sea surface reflection, including sunglint and whitecap, cause significant errors in the ocean color estimation [1,2,3]. Sea surface reflection can be estimated from a statistic scheme such as that presented by Cox and Munk [4] using low-resolution wind speed data from a microwave radiometer, a scatterometer, or objective analysis data (e.g., [5,6]). However, the correction based on the wind speed data is problematic in coastal areas because of fine variations in the distribution of surface reflection due to variable winds, fetch length, and air-sea stability caused by the fine structure of the coastal geography. Several studies have investigated high spatial resolution sunglint correction using hyperspectral bands or small scale glint variations (e.g. [7,8]). Murakami and Frouin [9] demonstrated the possibility of sunglint (ρ_g) correction by using 500-m resolution near infrared (NIR) and shortwave infrared (SWIR) bands of Moderate Resolution Imaging Spectroradiometer (MODIS). Higher (10-30 m) spatial resolution sensors are expected to capture higher resolution spatial structures of ocean color phenomena, especially in the coastal areas. However, they have a limited number of spectral bands generally (*e.g.*, without SWIR bands), which prevents the precise estimation of aerosol properties and the distinction between aerosol and sea-surface reflection.

In addition to these sensor limitations, coastal areas present difficulties for ocean color retrievals, *i.e.*, high NIR reflectance by suspended matter, complex Inherent Optical Properties (IOPs) due to various material inputs from the land, and bottom reflectance in the shallow areas. This explains why the blue/green ratio of remote sensing reflectance (R_{rs}), which is

traditionally used in the empirical estimation of chlorophyll-a concentration (*Chla*), does not allow to calculate *Chla* in most cases of the coastal area (see Table 1 for symbol definitions and units).

1.2 The New Caledonia lagoon

The New Caledonia lagoon is a large, almost continuous lagoon (22177 km^2) lying in the southwestern tropical Pacific from 20°S to 22°S and 166°E to 167°E (Fig. 1). Its heterogeneous bathymetry (25 m as a mean depth) is due to a complex geomorphology with the presence of sedimentary plains and a high proportion of shallow waters and numerous small sand islands [10,11,12]. It is largely connected to the open ocean along its southern side, but only by narrow passes in its southwestern side. It is an example of a coral reef lagoon system, which are very sensitive to anthropogenic (nutrients, mining) perturbations [10,11] as well as to interannual changes linked to the balance between dry El Niño and wet La Niña episodes [13,14], which are amplified in lagoons [12]. The central lagoon is characterized by oligotrophic to mesotrophic waters (yearly average chlorophyll-a concentration of 0.25 ± 0.01 mg m^{-3}) [15,16] and exhibits a strong seasonal cycle with higher values in austral winter (July) or austral summer (February) during nitrogen-fixing *Trichodesmium* blooms [17,18,19,20]. Upwelling at the barrier reefs [21] as well as internal waves in the southern part of the lagoon are two major mechanisms of exchange with the sea, which can modify the phytoplanktonic assemblage [22].

Rain can also induce large chlorophyll enrichments in the lagoon [23]. With relatively low river inputs and a low turbidity range (0.20-16 g m^{-3}), its trophic state is linked to spatial variations in flushing times [12,16,24]. Similarly to “optically complex” Case 2 European waters [25] or coastal bays [26], reflectance in the New Caledonia lagoon can be highly

variable [27] as in other tropical environments [28], the Australian Great Barrier Reef [29], tropical estuaries [30] with a high influence of mineral particles from river discharge in bays [31] or colored dissolved organic matter (CDOM) [32]. Additionally, bottom reflectance, which represents a strong component in clear tropical shallow waters, may influence R_{rs} [33,34,35,36].

In order to improve the challenge of remote sensing in coastal environments [37], surface water IOPs (absorption and backscattering) were measured during several observation campaigns (e.g., coastal stations of Diapalis in 2003, Bissecote, Echolag, Valhybio, and the Valhybio Monthly Survey cruises from 2006 to 2010) in the lagoon and at different seasons [27,38,39]. The bathymetry of the Southern New Caledonia lagoon was compiled [12].

1.3 ALOS AVNIR-2

Advanced Land Observation Satellite (ALOS) has been operated by JAXA from 24 Jan. 2006 to 12 May 2011 and carried the Advanced Visible and Near Infrared Radiometer type 2 (AVNIR-2). AVNIR-2 has four spectral bands (centered at 463 nm, 560 nm, 652 nm, and 821 nm) with a 10-m Instantaneous Field of View (IFOV), a 70-km Field of View (FOV) and a mechanical pointing function (by moving mirror) along the cross-track direction (±44 deg) for effective global land observation. To achieve the ALOS mission objectives (cartography, regional observation, disaster monitoring, resources survey, and technology development) and to expand to quantitative applications, such as determination of vegetation density, coastal water color and their time dependencies, it is important to evaluate, improve and maintain the radiometric calibration accuracy of AVNIR-2 (the pre-defined target is absolute error less than 10% [40]). The cross-calibration with MODIS indicated that the difference in top of

atmosphere (TOA) radiance is less than 3% in the visible bands, and the temporal stability of the radiance is less than 2% per 1000 days [41].

1.4 Scope of this study

Atmospheric and sea surface correction and IOP estimation were conducted using the four bands of 30-m images averaged from AVNIR-2 10-m images (see section 2.1). The linear matrix inversion (LMI) of IOPs [42,43,44] and atmospheric + surface reflection correction was simplified to allow the four-band and high spatial resolution AVNIR-2 retrievals. Influence of the bottom reflectance was reduced by using bathymetry data with a unique spectrum of bottom reflectance. We compared the IOP estimates by different candidate IOP spectra (observed particles + CDOM absorption (a_{pg}) and particle backscattering (b_{bp}) spectra) in the LMI scheme. *Chla* was estimated by two ways, from a statistical relationship with a_{pg}, or from blue/green ratio of R_{rs}. For the series of AVNIR2 images available over the New Caledonia lagoon, we validated the derived IOPs (a_{pg} and b_{bp}) and *Chla* using in situ measurements around the AVNIR-2 observation dates.

2. DATA AND METHODS

2.1 AVNIR-2 images and radiance correction

AVNIR-2 data have 10-m spatial resolution but only 8-bit digital resolution with relatively low gain designed for the land-surface observations. We averaged AVNIR-2 TOA radiance images to a 30-m (0.0003 degrees equal latitude-longitude) grid to reduce the sensor noise before the atmospheric correction because the ocean-color signal is much lower than atmospheric one in the visible wavelengths.

The AVNIR-2 in-orbit radiometric performance was evaluated through a comparison with Aqua MODIS by the cross-calibration scheme [41]. This scheme uses the TOA reflectance functions of the satellite zenith angle estimated by Aqua MODIS observations within ±16 days from the AVNIR-2 observation over temporally and spatially stable ground areas. The cross calibration with the Aqua MODIS over the Antarctic snow fields allow us to correct AVNIR-2 bands 1-4 by the correction coefficients shown in Table 2. We calculated the TOA reflectance of standard gas absorption conditions (column ozone = 343.8DU, water vapor = 14.19 mm, and pressure = 1013.25 hPa) from the AVNIR-2 radiance observation as shown in Appendix.

Seventeen clear AVNIR-2 scenes were captured around the target area in the ALOS mission period. The dates were 10 Sep. and 27 Sep. in 2006, 12 Feb., 3 Mar., 15 May, and 31 Jul. in 2007, 31 Oct. and 17 Nov. in 2008, 3 Sep. and 20 Nov. in 2009, 5 Jan., 3 Feb., 21 Mar., 8 Aug., and 22 Dec. in 2010, and 24 Mar. and 10 Apr. in 2011. Some scenes (27 Sep. 2006, 12 Feb. 2007, 31 Oct. and 17 Nov. 2008, 20 Nov. 2009, and 5 Jan. 2010) were covered by the sunglint. Match-ups with in situ measurements were obtained (total 15 points) on 3 Sep. 2009 (time difference from the AVNIR-2 observation ΔD=5 days), 17-18 Nov. 2009 (ΔD=2 days), and 11 Jan. 2010 (ΔD=6 days).

2.2 Simplification of the atmospheric and surface corrections

At each solar and sensor geometry condition, the TOA reflectance ρ_t,, for which gaseous absorption is normalized by standard atmosphere condition, can be described as follows.

$$\rho_t(\lambda_b) = \rho_r(\lambda_b) + \rho_a(\lambda_b, \tau_a, M) + t(\lambda_b, \tau_a, M)\times \rho_g(\lambda_b) + T(\lambda_b, \tau_a, M)\times \rho_{wc}(\lambda_b) + T(\lambda_b, \tau_a, M) \times \rho_w(\lambda_b) \quad (1)$$

where ρ_r is the atmospheric molecule reflectance, ρ_a is the aerosol reflectance, including aerosol-molecule interaction, ρ_w is the water-leaving reflectance, ρ_g is the sunglint reflectance, ρ_{wc} is the whitecap reflectance, t is the atmospheric direct transmittance (sun-surface + surface-satellite), and T is the direct + diffuse transmittance (sun-surface + surface-satellite), λ_b is the center wavelength of sensor spectral band, τ_a is the aerosol optical thickness, and M is the aerosol model. ρ_g can be estimated by a statistical equation [4] using wind speed and the refractive index of water at each wavelength. However, there is no simultaneous 30-m resolution wind speed data, and the statistical relation is not always consistent with the real complicated sea surface.

The Rayleigh scattering of ρ_r and T (at τ_a=0) can be estimated by atmospheric radiative transfer simulation. In order to achieve this, we used Pstar2b [45], which takes into account atmospheric polarization, provided by the National Institute for Environmental Studies (NIES) GOSAT project and the OpenCLASTR project [46,47,48]. We prepared look-up tables of $\rho_r(\lambda_b)$ (including sea-surface reflection with wind speed = 0) and T at each geometric condition.

The Rayleigh-scattering subtracted reflectance (ρ_{agw}) can be described by the following Eq. (2).

$$\rho_{agw}(\lambda_b) \equiv (\rho_t(\lambda_b) - \rho_r(\lambda_b)) / T(\lambda_b, \tau_a=0)$$

$$= [\ \rho_a(\lambda_b, \tau_a, M) / T(\lambda_b, \tau_a=0) + t(\lambda_b, \tau_a, M) / T(\lambda_b, \tau_a=0) \times \rho_g(\lambda_b) + T(\lambda_b, \tau_a, M) / T(\lambda_b, \tau_a=0) \times \rho_{wc}(\lambda_b)\ ] + T(\lambda_b, \tau_a, M) / T(\lambda_b, \tau_a=0) \times \rho_w(\lambda_b) \quad (2)$$

The $T(\lambda_{b=1,2,3 \text{ and } 4}, \tau_a=0)$ are about 0.83, 0.91, 0.95, and 0.98 respectively at $\theta_{sun}=\theta_{sat}=0$. $T(\lambda_b, \tau_a, M) / T(\lambda_b, \tau_a=0)$ can be approximated as 1.0 because it is >0.9 when τ_a<0.5. We simplified aerosol and surface reflection ($\rho_{ag} \equiv \rho_a + \rho_g$) as the following form (Eq. (3)) because ρ_{ag} is to

be spectrally smooth and can be approximated by a power function α of the wavelength ratio in most cases [49].

$$\rho_{ag}(\lambda_b) \cong \rho_{ag}(821\text{ nm}) \times (\lambda_b \times c_{wl} / 821\text{ nm})^{\alpha} \quad (3)$$

The spectral shape of ρ_{ag} was improved by a correction factor, c_{wl} (= 0.99 at band 3 (652 nm) and 1.0 at other bands), which was derived from the atmospheric radiative transfer simulation (the root mean square error of ρ_{ag} is 0.004 at 463 nm for the tropospheric, oceanic, and their mixed aerosols in the case of aerosol optical thickness = 0.3 and air-mass $pl < 4$). The α ranged from −0.5 to +0.3 for the oceanic aerosols and from −1.8 to −1.2 for the tropospheric aerosols.

The variables about the aerosol and surface reflection, α and ρ_{ag} (821 nm), could be estimated using the AVNIR-2 data through an iteration with the IOP retrieval described in the next section. The approximation of Eq. (3) enabled quick processing including the iteration scheme.

2.3 IOP and water-leaving reflectance estimation

Most of the IOP algorithms [50] are based on the equation of remote sensing reflectance below the surface (r_{rs}), the total absorption coefficient (a) and the backscattering coefficient (b_b) proposed by Gordon et al. [51].

$$r_{rs}(\lambda) = g_1 \times u(\lambda) + g_2 \times u(\lambda)^2 \quad (4)$$

$$a(\lambda) = a_w(\lambda) + a_{ph}(\lambda) + a_d(\lambda) + a_g(\lambda) \quad (5)$$

$$b_b(\lambda) = b_{bw}(\lambda) + b_{bp}(\lambda) \quad (6)$$

with

$$u(\lambda) = b_b(\lambda) / (b_b(\lambda) + a(\lambda)) \quad (7)$$

where g_1=0.0949 and g_2=0.0794 [51]. a_w, a_{ph}, a_d, and a_g are the absorption spectra of water, phytoplankton, detritus, and CDOM respectively. b_{bw} and b_{bp} are backscattering coefficients of water and particles. Remote sensing reflectance above the surface, R_{rs} is estimated from r_{rs} using the relation from [51,52] as:

$$R_{rs}(\lambda) = 0.52 \times r_{rs}(\lambda) / (1 - 1.7 \times r_{rs}(\lambda)). \quad (8)$$

The water-leaving reflectance ρ_w in (1) is simply calculated from the R_{rs}.

$$\rho_w(\lambda) = \pi \times R_{rs}(\lambda) \quad (9)$$

We used the LMI scheme [42,43,44] to estimate IOPs. The scheme requires a_w, b_{bw}, and model spectra, a_{ph}', a_{dg}' (absorption of detritus + CDOM), and b_{bp}', which is normalized at a specific wavelength (442 nm was used in this study). We used a_w and b_{bw} values from [53,54] weighted by the AVNIR-2 spectral response (shown in Table 3). Wavelength functions of a_{dg} and b_{bp} were as follows.

$$a_{dg}(\lambda_b) = a_{dg0} \times a_{dg}(\lambda)' \quad (10)$$

$$b_{bp}(\lambda_b) = b_{bp0} \times b_{bp}(\lambda_b)' \quad (11)$$

where

$$a_{dg}(\lambda)' = \exp(S \times (\lambda - 442)) \quad (12)$$

$$b_{bp}(\lambda)' = (\lambda / 442)^Y \quad (13)$$

where a_{dg0} is a_{dg} at 442 nm, b_{bp0} is b_{bp} at 442 nm, S= –0.010 or –0.018, and Y= –1.4, 0, or +2. S = –0.010 and Y = –1.4 were derived from the New Caledonia in situ measurements of a_{dg} and b_{bp} respectively.

191 The inversion process was simplified to use only two IOP parameters, a_{pg} ($\equiv a_p+a_g \equiv$
192 $a_{ph}+a_{dg}$) and b_{bp}, and two AVNIR-2 bands, band 1 (463 nm) and band 2 (560 nm). We set the
193 a_{pg}' as follows.

194 $$a_{pg}(\lambda_b) = a_{pg0} \times a_{pg}(\lambda_b)' = a_{pg0} \times \{ (1- r_{pg}) \times a_{ph}(\lambda_b)' + r_{pg} \times a_{dg}(\lambda_b)' \} \quad (14)$$

195 where a_{pg0} is a_{pg} at 442 nm. The ratio of a_{ph} and a_{dg} at 442 nm, r_{pg}, was set to 0.52 / (1 + 0.52)
196 considering the normal conditions observed in the New Caledonia in situ data [32]. We can
197 estimate two parameters of IOPs, a_{pg0} and b_{bp0}, by the iteration processes of the IOP forward
198 calculation and LMI [42,43,44].

199 If we have an initial value of a_{pg0} and b_{bp0}, ρ_w can be calculated by (4)-(14). Using the ρ_w,
200 ρ_{ag} at 652 nm and 821 nm can be calculated using molecular scattering corrected reflectance
201 derived from satellite observation (ρ_{agw}) as:

202 $$\rho_{ag}(\lambda) = \rho_{agw}(\lambda) - \rho_w(\lambda) \quad (15)$$

203 where λ = 652 nm and 821 nm. Considering an approximation of Eq. (3), α can be calculated
204 by Eq. (16).

205 $$\alpha = \log(\rho_{ag}(652 \text{ nm}) / \rho_{ag}(821 \text{ nm})) / \log(652 \times c_{wl} / 821) \quad (16)$$

206 Then, ρ_w at 463 nm and 560 nm are calculated by Eqs. (3) and (15). Using the ρ_w at the two
207 visible bands, a_{pg0} and b_{bp0} can be calculated by the LMI [42,43,44].

208 The iteration process to derive the final value of a_{pg0} and b_{bp0} is shown in Fig. 2. The first
209 process aims to estimate α except for shallow areas (bathymetry<20m) where the bottom
210 reflectance can influence r_{rs}. The iteration was repeated to find optimal values of a_{pg0} and b_{bp0}

by minimizing the difference between b_{bp0} preset in Eq. (11) and b_{bp0} calculated by the inversion matrix. The initial value of a_{pg0}' was set to 0.01, which does not affect the final a_{pg0} estimates because a_{pg} is relatively small in the total a in red and NIR wavelengths. The sub-process is repeated until $| a_{pg0} - a_{pg0}' | < 0.0001$ (practically less than four times in most pixels) with revision of a_{pg0} and the search range of b_{bp0} ($b_{bp0}^{(max)}$) which is set by ρ_{ag} at 821 nm and the extremely high a_{pg0} = 20 m^{-1}. After completing the first process, we smoothed α for each 0.1 deg × 0.1 deg area to reduce the AVNIR-2 sensor noise and extrapolate to the shallow (<20m) areas where we did not estimate α in the first process. The second process derives ρ_{ag} a_{pg}, b_{bp}, and R_{rs} for every 30-m grid using the same equations. We can derive IOPs and R_{rs} at any wavelengths (AVNIR-2 bands at 463 nm and 560 nm and the wavelengths of the in situ measurements at 442 nm and 555 nm) using the IOP spectra $a_{pg}(\lambda)$' and $b_{bp}(\lambda)$' (see section 2.5).

2.4 Chlorophyll-a estimation

Chlorophyll-a was estimated by regression of a_{pg}(442 nm) and the empirical blue/green as follows:

$$\log_{10}(Chla) = 0.9706 + 1.1835 \times \log_{10}(a_{pg}(442\ \text{nm})) \quad (17)$$

$$\log_{10}(Chla) = 0.1464 - 1.7953\, r + 0.9718\, r^2 - 0.8319\, r^3 - 0.8073\, r^4 \quad (18)$$

where

$$r = \log_{10}(R_{rs}(463\ \text{nm}) / R_{rs}(560\ \text{nm})). \quad (19)$$

The relationship between *Chla* and a_{pg}(443 nm) was derived from a_{pg} and the fluorometric chlorophyll-a data included in the bio-Optical Marine Algorithm Data set (NOMAD) [55] (Fig. 3). The MODIS OC2M-HI equation developed by the NASA Ocean Biology Processing Group

(OBPG) using the NOMAD database [6] was used for the two channel equation because AVNIR-2 has only two channels in blue and green wavelengths.

2.5 In situ bio-optical measurements

Field measurements of the two IOPs, the absorption coefficient, a, and the backscattering coefficient, b_b, were obtained at stations in the southwest part of the lagoon (Fig. 1) during various seasons from 2006 to 2010. The b_b was measured with a Hydroscat-6 profiler (H6: HobiLabs, wavebands (λ) centered at 442, 488, 510, 550, 620 and 670 nm with a bandwidth of 10 nm for the 442–550 nm bands and 20 nm for the 620 and 670 nm bands) [19,27]. The particulate back-scattering coefficient, $b_{bp}(\lambda)$, was calculated by subtracting from $b_b(\lambda)$ the theoretical "pure water spectrum", $b_{bw}(\lambda)$ (calculated as $b_{bw}(\lambda) = 0.5\times\ b_w(\lambda)$) [51]. The particulate absorption coefficient, $a_p(\lambda)$, was measured with the filter-pad technique [56] using water samples filtered onto 25-mm GF/F Whatman filters. For pigments, the filters were dipped in 5.4 ml 100% acetone (final concentration 90% acetone taking into account water retention by the filter, e.g., 0.621 ± 0.034 ml) and ground with the freshly broken end of a glass rod for chlorophyll and phaeopigment extraction [57]. For comparison with the satellite-estimated *Chla*, we used the sum of chlorophyll a and divinyl chlorophyll a, *Chla* (in mg m^{-3}), as measured by spectrofluorometry, and well correlated with fluorometry in the Caledonian lagoon [15,27].

For the LMI, we prepared the model spectra of a_{pg} and b_{bp} optimized for the New Caledonia in situ samples (six samples of a_{ph} and a_{dg} in 2003, and 112 samples of b_{bp} in 2006-2010). The samples of a_{ph} and a_{dg} were distributed around the lagoon of the southeast New Caledonia, but not near bays of the mainland. The spectral shape a_{dg}' and b_{bp}' (relative values

255 from λ=442 nm) were modeled by Eqs. (12) and (13) respectively. The model spectra from the
256 averages of the New Caledonia measurements were used as the standard in sensitivity tests
257 described below.

258 We tested the sensitivity of different sets of model spectra: (A) a_{pg}' and b_{bp}' from the New
259 Caledonia measurements (e.g., same as the above); (B) same as (A) but a_{ph}' from a
260 picoplankton spectra [58]; (c) same as (A) except for a_{ph}' from a microplankton spectra [58];
261 (D) same as (A) except for a_{dg}' with S = –0.018; (E) same as (A) except for b_{bp}' with Y = 0.0;
262 and (F) same as (A) except for b_{bp}' with Y = –2.0 (Fig. 4). These a_{ph}' spectra are listed in Table
263 3.

264 ## 2.6 Correction of sea floor reflection

265 The R_{rs} and IOP estimation might be influenced by bottom reflectance especially in low
266 absorption and shallow areas, such as site G003 near the barrier reef (11 meters depth, bottom
267 composed of white sands). r_{rs} in shallow areas was approximated by the following equation
268 from [59]:

269 $$r_{rs} \sim r_{rs}^{dp} \times [1 - \exp\{ -\kappa H \times (1 / \cos\theta_{0w} + D_u^C / \cos\theta_w) \}]$$

270 $$+ \rho_b / \pi \times \exp\{ -\kappa H \times (1 / \cos\theta_{0w} + D_u^B / \cos\theta_w) \} \quad (20)$$

271 where ρ_b is the bottom albedo, H is the bottom depth, θ_{0w} is the subsurface solar zenith angle,
272 θ_w is the subsurface viewing angle from nadir ($\theta_w = \sin^{-1}(1 / 1.34 \times \sin \theta_a)$, θ_a is the above-
273 surface angle), r_{rs}^{dp} is the remote-sensing reflectance for optically deep water, and κ is the
274 attenuation coefficient ($\kappa(\lambda) = a(\lambda) + b_b(\lambda)$). D_u^C and D_u^B are optical path-elongation factors

for scattered photons from the water column and bottom respectively, which are described by functions of $u(\lambda)$ following [59].

Because ρ_b is unknown at each image grid in this study, we used a ρ_b spectrum of coral sand shown by Fig. 6 of [60] (ρ_b = 0.33 and 0.47 at 442nm and 555nm respectively). The similar ρ_b spectra of the sandy sea bottom were reported around the coral reef system by [61,62]. We use H compiled in [12] (Fig. 5). Attenuation coefficient, $\kappa(\lambda)$, is iteratively calculated through the IOP estimation described in section 2.3 by changing H from enough deep depth (1000m) to the actual sea-floor depth gradually. Such an approach has been used to retrieve bathymetry [36].

2.7 MODIS ocean color products

NASA OBPG Aqua MODIS products, R_{rs} at 443 nm, R_{rs} at 555 nm, and *Chla* (processing version 2009.1) [6], were used for the comparison to our results. The global accuracies of the MODIS data set, reported as the median absolute percent differences of normalized water-leaving radiance (L_{wn}) at 443 nm, L_{wn} at 555 nm, and *Chla* from global in situ observations, are 18%, 17%, and 37% respectively [6,63]. We selected clear MODIS scenes ±1 day from AVNIR-2 observations or between the AVNIR-2 and in situ observation dates.

3. RESULTS

3.1 R_{rs} and ρ_{ag}

Figure 6 shows results of the ρ_{agw} (463 nm), ρ_{ag} (463 nm), α, ρ_w (463 nm) without bottom correction, and ρ_w (463 nm) with bottom correction on 17 Nov. 2008 and 3 Sep. 2009. On 17 Nov. 2008, the area was covered by sunglint (brighter on the right side in Figs. 6a and 6b). ρ_{ag} (Fig. 6b) showed small-scale structures of the surface reflection caused by the winds and

297 geographical features. α (Figs. 6c and 6h) was smoothed in each 0.1 deg × 0.1 deg grid after
298 the first process ((a) in Fig. 2). The estimated ρ_w (Fig. 6d) was very smooth offshore and
299 showed fine structures inside the lagoon. On 3 Sep. 2009, aerosol with small clouds extended
300 northwest to southeast over the area (Fig. 6g). The aerosol pattern was removed effectively in
301 the ρ_w image (Fig. 6i) by subtracting ρ_{ag} (Fig. 6g) from ρ_{agw} (Fig. 6f). High reflectance areas
302 remained inside the lagoon with a dark area along the outside of the barrier reef.

303 The comparison between AVNIR R_{rs} and MODIS R_{rs} at 442nm (or 443 nm) and 555 nm is
304 shown in Fig. 7. AVNIR-2 R_{rs} at 555nm appears slightly higher, but the results are closely
305 correlated (0.77 and 0.54 at 442 nm and 555 nm, respectively, and the Root Mean Square
306 Difference (RMSD) was about 40% and 63% of the average R_{rs} for AVNIR-2 and MODIS,
307 respectively) except for some samples at the shallow stations (*e.g.*, B50 and B03). An outlier at
308 station G003 in Fig 7a (AVNIR-2 R_{rs} at 442 nm is about 0.03) seemed to be influenced by
309 cloud edge in the AVNIR-2 image on 31 Jul. 2007.

310 Figures 6e and 6j show the AVNIR-2 ρ_w at 463nm with the correction of bottom
311 reflectance. The correction decreases ρ_w inside of the lagoon (*e.g.*, at stations M33 and G003)
312 and reduces the pattern of the bathymetry (seen Fig. 5) in most areas in the ρ_w images.
313 However, it seems to cause overcorrection in some areas, *e.g.*, around the islands and the
314 barrier reef.

315 ### 3.2 a_{pg} and b_{bp}

316 Figures 8a and 8b shows a_{pg} at 442nm and b_{bp} at 555nm without the bottom correction
317 (using model spectra (A) in Table 4). a_{pg} was high along the coast and in bays near the main
318 land. On the other hand, b_{bp} was high inside the lagoon especially at shallow bottom areas (e.g.,

G003). Scatter plots between the in situ ($a_p \times 1.52$) and the AVNIR-2 a_{pg} and b_{bp} estimates are shown in Figs. 9a and 9b. They show that AVNIR-2 a_{pg} is well correlated with in situ values for a_{pg} (r = 0.91 in Fig. 9a) even though the factor 1.52 may vary with changing proportions of a_p or a_g in $a_{pg} = a_p + a_g$. AVNIR-2 b_{bp} showed a high correlation coefficient (about 0.94 at 555 nm), but some values of b_{bp} were higher than the in situ b_{bp}. The overestimated samples were found in shallow areas (3.6 m, 6 m, 5m, and 11 m at stations B50, B03, Ile aux Canards and G003 respectively).

Figures 8c and 8d show a_{pg} and b_{bp} with the bottom reflectance correction on 3 Sep 2009. The correction decreased a_{pg} and b_{bp} in the lagoon areas. The comparison to the in-situ observations (Figs. 9c and 9d) showed that the correction improved the agreement especially at stations M33, Ile aux Canards, and G003 where the bottom depth is shallow and a_{pg} is relatively low. The AVNIR-2 a_{pg} was still higher than the in-situ a_{pg} at stations B50 and B03 around the Boulari Bay. Bias of a_{pg} (b_{bp}) were improved from 0.188 to 0.118 (from 0.023 to 0.015), and RMSD of a_{pg} (b_{bp}) from 0.489 to 0.290 (from 0.042 to 0.025) by the bottom correction.

Table 4 shows the results for the fifteen match-ups by using different spectra of a_{pg} and b_{bp}. Superscripts – and + show results with smaller or larger bias or RMSD (statistically significance level of 95%) than ones by the model spectrum (A). The results depended on the model spectra significantly, and the model (D) brought the smallest RMSD of both a_{pg} and b_{bp} with the bottom reflectance correction. Note that the microplankton for a_{ph} [58] gives larger RMSD than the measured around New Caledonia. Similarly, a slope of $Y = -2$ is too different from those measured and would not allow a proper retrieval of IOPs from AVNIR-2. Figures

9e-9h show the scatter plots by the model spectrum (D). RMSDs of a_{pg} and b_{bp} are significantly decreased (especially stations B50 and B03) by the optimal model spectrum.

3.3 Chlorophyll-a concentration

Figures 10 and 11 show the comparison among *Chla* estimated from a_{pg} (by the optimal model (D)), *Chla* calculated by OC2M-HI (using R_{rs} by AVNIR-2), and the MODIS standard (OC3M) 1-km *Chla*. *Chla* estimated from a_{pg} (Figs. 10a and 11a) was slightly smaller than *Chla* determined by other algorithms in the lagoon areas (*e.g.*, sites B08 and Ile aux Canards in Figs. 10 and 11). The AVNIR-2 OC2M-HI *Chla* was larger than indicated by the in situ data and similar to the MODIS standard value in the lagoon (see around sites M33 and G003 in Figs. 10b, 10e, and Figs. 11b and 11e). The scatter plots show that *Chla* from a_{pg} provides the best agreement among the three methods in the lagoon (RMSD=0.47, 0.61, and 0.60 in Figs. 10a, 10b, and 10e). The MODIS data at stations M33 and GD10 were scattered because they were too near the coast or the lagoon islands compared to the 1-km resolution products.

Figures 11c and 11d show results with the bottom correction. OC2M-HI *Chla* (Fig. 11d) was calculated by R_{rs} from r_{rs}^{dp} (Eq. (8)). Usual high biases of a_{pg} and b_{bp} in the shallow areas (B50, B03, and Ile aux Canards) around lagoon islands were decreased by the correction (Figs. 8c and 8d). It reduced overestimate of *Chla* by both a_{pg} and OC2 schemes, and improved the agreement with the in-situ matchups inside the lagoon (Figs. 10c and 10d).

4. DISCUSSION

4.1 a_{pg} and b_{bp} spectra

Agreement with in situ data was dependent on spectra of a_{pg} and b_{bp} (Table 4). For example, the a_{ph} spectrum of microplankton [58] (model C) and b_{bp} spectrum of Y=−2.0 (F) caused worse results than the spectrum modeled from New Caledonia in situ measurements (A) (Table 4). The agreement may be improved further if we optimize the spectra to more specific water types, *e.g.*, bays near the main land, middle-lagoon waters, and waters outside of the barrier reef (*e.g.*, open ocean). For example, modification of spectral slope of a_{dg} improved the IOP estimate especially around the Boulari Bay (model (D) in Fig. 9). The accuracies of the best results (r=0.91 and r=0.75 in Figs. 9g and 9h respectively) were better than ones by Quasi-Analytical Algorithm (QAA) [52,64] by using 1km MODIS Aqua Rrs data (r=0.84 and 0.72 for a_{pg} 443nm and b_{bp} 555nm respectively (Figures of QAA results are not shown here).

Such an optimization with the best-candidate spectra can be a useful way to obtain locally-optimized environmental monitoring from satellite observations with theoretical understanding of the local optical environment.

This study cannot determine spectral models such as the ratio between a_p and a_g (or a_{ph} and a_{dg}), because AVNIR-2 has only two channels in the blue and green wavelengths. More bands at 250 m to 300 m of spatial resolution from sensors such as SGLI and OLCI may be able to improve the discrimination of the IOPs.

The IOP retrieval schemes have been developed for observations by narrow (about 10-20nm) band-width sensors, estimates of absorption coefficients by the wide band can cause errors reaching about 20% [65] by the QAA [52,64] through the integration of the IOP spectra

in the band wavelengths. Our estimates rely on relatively wide bands (about 90nm) of AVNIR-2. We confirmed our retrieval of a_{pg} by the LMI can change about 20% (mostly overestimated) using simulated *Rrs* from our in-situ a_{pg} and b_{bp}. The error is still much smaller than the error due to difference of the model IOP spectra, however, it will need to be considered for more precise estimate in the future.

4.2 Aerosol and sea surface reflection estimation

Most of the iteration schemes for the atmospheric correction use the relationship between NIR R_{rs} and *Chla*. This study uses the relationships among a_{pg}, b_{bp}, ρ_{ag}, and α based on the convergence of b_{bp}. This scheme can avoid negative IOPs by tuning the aerosol parameters α and ρ_{ag} in the iteration process. Another merit of this aerosol estimation is the fast processing time (2-3 minutes for our study area (2001×1334 pixels) by a wide-use PC Linux machine) because it does not require time to access the aerosol look-up table that is used in the standard ocean color atmospheric correction algorithms.

The New Caledonia lagoon area has a relatively clear atmosphere compared to coasts in the northern hemisphere, such as the Asian coasts. This scheme does not consider absorptive aerosols that cannot be described by the simple Eq. (3). For more complex atmosphere (aerosol) conditions, more bands may be necessary than the two that were used here for the aerosol characterization (this study used 652 nm and 821 nm). If the sensor has lower noise and SWIR bands (e.g., MODIS 500 m bands and SGLI 250m band), we may be able to estimate α at each pixel and obtain more realistic measurements of α and ρ_{ag}. However, the absorptive aerosol correction may still be difficult using the simple Eq. (3).

4.3 The bottom effect

AVNIR-2 b_{bp} seemed to be influenced by the bottom reflectance. Bottom sands can be seen from satellite if bathymetry is shallow. For example, the bottom depth of the station G003 is 11 m with a relatively low a_{pg}. Agreement between AVNIR-2 IOPs and in situ IOPs were improved by considering the bottom reflectance generally, but they seemed to be overcorrected in some areas around the islands and along the barrier reef (Fig 6j). They are supposed to be influenced by coverage of live corals or sediment from the land, which may cause a different spectrum of the bottom reflectance from the coral sand reflectance [60,61,62]. This indicates that our IOP estimation could be improved if the precise bottom depth and real bottom reflectance are used [36].

4.4 Cloud shadow and adjacent scattering

For the 10-m resolution data, it is important to consider cloud shadow and sea surface reflection of scattered light from the cloud bottom. Identification of clouds around the coast (including over the land) and geometric calculation considering the cloud height are required. In addition, the clouds and land area can influence the coastal ocean color estimation, which is known as the adjacent effect [66]. The influence of the cloud shadow seemed to affect b_{bp}, but not a_{pg} as observed in the southeastern part of Fig. 8. Further study is needed to determine b_{bp} in the absence of the influence of the cloud effects.

5. CONCLUSION

This study investigated the correction of atmospheric scattering and sea surface reflection in the southwest region of the New Caledonia lagoon using AVNIR-2 images, which have four bands from visible to NIR wavelengths with 10-m resolution (our processing was conducted

after averaging for 30-m (3×3) grids). We applied corrections for gas absorption, molecule scattering, and $\rho_a + \rho_g$ using the iteration scheme for converging b_{bp} through IOPs from visible bands. This scheme was able to correct fine structure patterns of the $\rho_a + \rho_g$ successfully. The AVNIR-2-estimated R_{rs} agreed well with the MODIS R_{rs} (root-mean square difference / average of R_{rs} at 443 nm = 40%). Future projects, e.g., the Global Change Observation Mission (GCOM), using the Second-generation Global Imager (SGLI) and the Sentinel-3 Ocean and Land Colour Imager (OLCI), will have finer (250 m - 300 m) spatial resolution aiming for coastal monitoring with a swath of more than 1150 km. These missions will require a correction of the surface reflection with high spatial resolution and a reduction of masked areas in order to increase the observation frequency in the coastal areas.

With the bottom correction, the AVNIR-2-estimated IOPs agreed well with in situ IOP measurements (correlation coefficients were more than 0.9). Overcorrection appeared in the muddy bays and along the barrier reef, and it suggested that a constant bottom reflectance was not applicable in these areas.

This study showed that the AVNIR-2-estimated *Chla* from the a_{pg} regression scheme in the lagoon area does not show the overestimation observed with the blue / green R_{rs} ratio. This also confirms that the relationship between *Chla* and a_{pg} in the lagoon area is not different from the a_{pg}-*Chla* relationship of the NOMAD database as already shown in [27]. The NOMAD relationship cannot be used in bays (*e.g.*, B50), where the a_{pg}-*Chla* relationship is disturbed by absorbing mineral particles and irregular a_g due to river discharge.

Our atmospheric correction and IOP estimation scheme which requires only four bands in the visible and NIR wavelengths can be applied to other satellite sensors, such as the MODIS

500-m bands, and other multi-band sensors, such as SGLI 250-m bands. The performance depends on the candidate spectra of IOPs based on in situ measurements (and aerosols) in the target areas. This reinforces the need to construct databases of the various spectra of IOPs and aerosols in various regions through international collaboration to develop globally applicable approaches. The target of this study is not to make a fixed algorithm, but demonstrate the method to make local optimal estimate of the IOPs and *Chla*. So, the algorithm should not be applied elsewhere without a similar effort *i.e.*, preparation of the candidate spectra for the target areas.

ACKNOWLEDGEMENTS

The authors are grateful to the OpenCLASTR project and the NIES GOSAT project for the use of the Rstar6b and Pstar2b packages in this research. MODIS L2 R_{rs} and chlorophyll-a data were provided by NASA OBPG. OMI ozone data were provided by the Goddard Space Flight Center. NCEP wind speed and sea level pressure data were provided by the NCEP/NCAR Reanalysis Project. ALOS AVNIR-2 data were provided by the JAXA EORC ALOS research and application project. In situ data were obtained in the frame of INSU PNTS ValHyBio and processed using the SeaDAS and home package. The a_{pg}-*Chla* relationship was calculated using NOMAD Version 2.0 ALPHA, which was compiled by the NASA OBPG, Goddard Space Flight Center.

APPENDIX:

Calculation of TOA reflectance with gaseous absorption correction

$$\rho_t(b) = L_{avnir2}(b) / f_{vc}(b) \times \pi \times d^2 / F_0(b) / \cos(\theta_{sun}) / t_{oz} / t_{wv} / t_{O2} \quad \text{(A1)}$$

where $t_{oz} = \exp(-k_{oz}(b) \times (oz - 343.8) \times pl)$ (A2)

$$t_{wv} = \exp(-\{ k_{wv}(b) \times (ptw - 14.19) \times pl + k_{wv2}(b) \times ((ptw \times pl)^2 - (14.19 \times pl)^2) \}) \quad \text{(A3)}$$

$$t_{O2} = \exp(-k_{O2}(b) \times (prs - 1013.25) \times 0.2095 \times pl) \quad \text{(A4)}$$

$$pl = 1 / \cos(\theta_{sun}) + 1 / \cos(\theta_{sat}) \quad \text{(A5)}$$

L_{avnir2} is the AVNIR-2-observed radiance [W/m^2/μm/sr], b represents the AVNIR-2 spectral bands, f_{vc} is the vicarious calibration factor defined as ratio of AVNIR-2 radiance to radiance simulated by MODIS observation, d is the sun-earth distance [AU], F_0 is the solar irradiance at 1 AU [67], θ_{sun} is the solar zenith angle [rad], θ_{sat} is the satellite zenith angle [rad], oz is the column ozone [DU], ptw is the column water vapor [mm], and prs is the sea-level pressure [hPa]. The gas absorption coefficients k_{oz}, k_{wv} and k_{O2} were calculated by MODTRAN 4 [68] considering the spectral response of the AVNIR-2 bands (Table 2). We used ptw and prs from the National Centers for Environmental Prediction (NCEP) and oz from the Ozone Monitoring Instrument (OMI), which is distributed by Goddard Space Flight Center.

REFERENCES

1. R. Frouin, M. Schwindling, and P. Y. Deschamps, "Spectral reflectance of sea foam in the visible and near infrared: in situ measurements and remote sensing implications," *Journal of Geophysical Research, 101*, 14361-14371 (1996).
2. K. D. Moore, K. J.Voss, and H. R. Gordon, "Spectral reflectance of whitecaps: their contribution to water-leaving radiance", *Journal of Geophysical Research*, 105, 6493-6499 (2000).

3. J.-M. Nicolas, P.-Y. Deschamps, and R. Frouin, “Spectral Reflectance of Oceanic Whitecaps in the Visible and near Infrared: Aircraft Measurements Over Open Ocean,” *Geophysical Reearch Letter*, ***28*** *(23)*, 4445-4448 (2001).

4. C. Cox, and W. Munk, “Measurements of the roughness of the sea surface from photographs of the sun’s glitter,” *Journal of the Optical Society Of America.*, 44, 838-850 (1954).

5. M. Wang, and S.W. Bailey, “Correction of sun glint contamination on the SeaWiFS ocean and atmosphere products,” *Applied Optics*, 40, 4790-4798 (2001).

6. G.C. Feldman, “The OC2 algorithm for MODIS,” Seadas Forum, NASA-GSFC, NASA OceanColor webpage http://oceancolor.gsfc.nasa.gov/REPROCESSING/R2009/.

7. E. Hochberg, S. Andrefouet, and M. Tyler, “Sea Surface Correction of High Spatial Resolution Ikonos Images to Improve Bottom Mapping in Near-Shore Environments,” *IEEE Trans. Geosci. Remote Sens.*, 41, 1724-1729 (2003).

8. J. A. Goodman, Z-P. Lee, and S. L. Ustin, “Influence of Atmospheric and Sea-Surface Corrections on Retrieval of Bottom Depth and Reflectance Using a Semi-Analytical Model: A Case Study in Kaneohe Bay, Hawaii,” *Appl. Optics*, 47, F1-F11 (2008).

9. H. Murakami, and R. Frouin, “Correction of sea surface reflection in the coastal area,” *Proc. SPIE* Vol. 7150-4, Remote Sensing of Inland, Coastal, and Oceanic Waters edited by R. Frouin, *Proc. SPIE Asia-Pacific Remote Sensing*, 17-21 November 2008, Nouméa, New Caledonia (2008).

10. R. Fichez, L. Breau, C. Chevillon, S. Chifflet, P. Douillet, V. Faure, J.M. Fernandez, P. Gérard, L. Hédouin, A. Lapetite, S. Ouillon, O. Pringault, and J.P. Torréton, “Origine,

transport et devenir des apports naturels et anthropiques dans le lagon sud-ouest de Nouvelle-Calédonie," *Journal de la Société des Océanistes*, 126-127, 41-58 (2008).

11. R. Fichez, S. Chifflet, P. Douillet, P. Gerard, F. Gutierrez, A. Jouon, S. Ouillon, and C. Grenz, "Biogeochemical typology and temporal variability of lagoon waters in a coral reef ecosystem subject to terrigeneous and anthropogenic inputs (New Caledonia)," *Marine Pollution Bulletin,* 61, 7-12, 309-322 (2010).
12. S.Ouillon, P.Douillet, J.P. Lefebvre, R. Le Gendre, A. Jouon, P. Bonneton, J.M. Fernandez, C. Chevillon, O. Magand, J. Lefevre, P. Le Hir, R. Laganier, F. Dumas, P. Marchesiello, A. Bel Madani, S. Andrefouet, J.Y. Panche, and R. Fichez, "Circulation and suspended sediment transport in a coral reef lagoon: the southwest lagoon of New Caledonia," *Marine Pollution Bulletin,* 61, 7-12, 269-296 (2010).
13. J.Lefèvre, P. C. Marchesiello, N. C. Jourdain, C. Menkes, and A. Leroy, "Weather regimes and orographic circulation around New Caledonia," *Marine Pollution Bulletin,* 61, 413-431 (2010).
14. R.Fuchs, C. Dupouy, P. Douillet, F. Dumas, M. Caillaud, A. Mangin, and C. Pinazo, "Modelling the impact of a La Niña event on a South West Pacific Lagoon," *Marine Pollution Bulletin* (2012) *in press*.
15. J. Neveux, M.M.B. Tenorio, S. Jacquet, J.-P. Torreton, P. Douillet, S. Ouillon, and C. Dupouy, "Chlorophylls and phycoerythrins as markers of environmental forcings including cyclone Erica effect (March 2003) on phytoplankton in the southwest lagoon of New Caledonia and oceanic adjacent area," *International J. Oceanogr., Article ID 23251*, doi:10.1155/2009/232513 (2009).

16. J.P. Torréton, E. Rochelle-Newall, O. Pringault, S. Jacquet, V. Faure, E. Briand, "Variability of primary and bacterial production in a coral reef lagoon (New Caledonia)," *Mar Pollut Bull*, **61**, 335-348 (2010).
17. C. Dupouy, G. Dirberg, J. Neveux, M. Tenorio, and A. Le Bouteiller, "The contribution of T*richodesmium* to inherent optical properties of a tropical oligotrophic archipelago," in: Conference CD-ROM ''OCEAN OPTICS XVII", 26 October–3 November 2004, Fremantle, Australia, 3pp (2004).
18. C. Dupouy, D. Benielli-Gary, Y. Dandonneau, J. Neveux, G. Dirberg, and T. Westberry, "On the feasibility of detecting *Trichodesmium* blooms with SeaWiFS in the South Western Tropical Pacific," Remote Sensing of Inland, Coastal, and Oceanic Waters. *Proceedings of SPIE*, vol. 7150. SPIE, Bellingham, WA [7150 37] 715010, 9pp (2008).
19. C. Dupouy, J. Neveux, G. Dirberg, M.M.B. Tenorio, R. Rottgers, and S. Ouillon, "Bio-optical properties of marine cyanobacteria *Trichodesmium*, spp.," *Journal of Applied Remote Sens.* 2, 023503 (2008).
20. C. Dupouy, D. Benielli-Gary, J. Neveux, Y. Dandonneau, and T. Westberry, "A new algorithm for detecting Trichodesmium surface blooms in the South Western Tropical Pacific," *Biogeosciences*, 8, 1-17 (2011).
21. A. Ganachaud, A. Vega, M. Rodier, C. Dupouy, C. Maes, P. Marchesiello, G. Eldin, K. Ridgway, and R. Le Borgne, "Observed impact of upwelling on water properties and biological activity off the southwest coast of New Caledonia," *Marine Pollution Bulletin*, 61, 449-464 (2010).
22. J. Neveux, J.-P. Lefebvre, R. Le Gendre, C. Dupouy, F. Gallois, C. Courties, P. Gerard, S. Ouillon, and J.M. Fernandez, "Phytoplankton dynamics in New-Caledonian lagoon during

555 a southeast trade winds event," *Journal Marine Systems*, 82, 230-244, doi:10.1016/
556 j.jmarsys.2010.05.010 (2010).
557 23. C. Dupouy, A. Minghelli-Roman, M. Despinoy, R. Röttgers, J. Neveux, S. Ouillon, C.
558 Pinazo, and M. Petit, "MODIS/Aqua chlorophyll monitoring of the New Caledonia
559 lagoon: the VALHYBIO project," in *Proceedings of SPIE*, Vol. 7150 (SPIE, Bellingham,
560 WA, 2008) [7150 41] 715014, 8 pp (2008).
561 24. R. Fuchs, C. Pinazo, P. Douillet, C. Dupouy, and V. Faure, "New Caledonia Surface
562 lagoon chlorophyll modeling as coastal reef area health indicator," in "*Remote sensing of*
563 *the coastal ocean, land, and atmosphere environment*" edited by Robert J. Frouin, Proc.
564 SPIE Vol. AE103 (SPIE, Bellingham, WA, 2010) [7858 20], 9 pp (2010).
565 25. M. Babin, D. Stramski, G.M. Ferrari, H. Claustre, A. Bricaud, and G. Obolenski,
566 "Variations in the light absorption coefficients of phytoplankton, non-algal particles, and
567 dissolved organic matter in coastal waters around Europe," *Journal of Geophysical*
568 *Research*, 108. doi:10.1029/2001JC000882 (2003).
569 26. C.M. Hu, Z.Q. Chen, T.D. Clayton, P. Swarzenski, J.C. Brock, and F.E. Muller-Karger,
570 "Assessment of estuarine water-quality indicators using MODIS medium resolution bands:
571 initial results from Tampa Bay, FL.," *Remote Sensing of Environment*, 93, 423–441 (2004).
572 27. C. Dupouy, J. Neveux, S. Ouillon, R. Frouin, H. Murakami, S. Hochard, and G. Dirberg,
573 "Inherent optical properties and satellite retrieval of chlorophyll concentration in the
574 lagoon and open ocean waters of New Caledonia," *Marine Pollution Bulletin 61*, 503–518,
575 doi:10.1016/j.marpolbul.2010.06.039 (2010).

576 28. J.G. Acker, A. Vasilkov, D. Nadeau, and N. Kuring, “Use of SeaWiFS ocean color data to
577 estimate neritic sediment mass transport from carbonate platforms for two hurricane-
578 forced events,” *Coral Reefs,* 23, 39–47 (2004).
579 29. D. Blondeau-Patissier, V.E. Brando, K. Oubelkheir, A.G. Dekker, L.A. Clementson, and P.
580 Daniel, “Bio-optical variability of the absorption and scattering properties of the
581 Queensland inshore and reef waters, Australia,” *Journal of Geophysical Research,* 114,
582 C05003,doi:10.1029/2008JC005039 (2009).
583 30. K. Oubelkheir, L.A. Clementson, I.T. Webster, P.W. Ford, A.G. Dekker, L.C. Radke, and
584 P.Daniel, “Using inherent optical properties to investigate biogeochemical dynamics in a
585 tropical macrotidal coastal system,” *Journal of Geophysical Research,* 111, C07021
586 doi:10.1029/2005JC003113 (2006).
587 31. S. Ouillon, P. Douillet, A. Petrenko, J. Neveux, C. Dupouy, J.-M. Froidefond, S.
588 Andréfouët, and A. Muñoz-Caravaca, “Optical Algorithms at Satellite Wavelengths for
589 Total Suspended Matter in Tropical Coastal Waters,” *Sensors,* 8, 4165-4185; doi:
590 10.3390/s8074165 (2008).
591 32. C. Dupouy, and R. Roettgers, “Absorption by different components during a high
592 freshwater event of the 2008 La Nina episode in a tropical lagoon,” Poster Session “Bio-
593 optics and biogeochemistry”, *Ocean Optics XX,* Anchorage (Alaska), 25-30 September
594 2010 (2010).
595 33. Z-P. Lee, K.L. Carder, R.F. Chen, and T.G. Peacock, “Properties of the water column and
596 bottom derived from Airborne Visible Infrared Imaging Spectrometer (AVIRIS) data,”
597 *Journal of Geophysical Research,* 106, 11639–11651 (2001).

598 34. J.P. Cannizaro, and K.L. Carder, “Estimating chlorophyll a concentrations from remote-
599 sensing reflectance in optically shallow waters,” *Remote Sensing of Environment*, 101, 13–
600 24 (2006).
601 35. A. Minghelli-Roman, L. Polidori, S. Mathieu-Blanc, L. Loubersac, and F. Cauneau,
602 “Bathymetric estimation using MeRIS images in coastal sea waters,” *IEEE Transactions*
603 *Geosciences Remote Sensing*, 4, 274–277 (2007).
604 36. A. Minghelli-Roman, C. Dupouy, C. Chevillon, P. Douillet, “Bathymetry retrieval and sea
605 bed mapping in the lagoon of New Caledonia with MeRIS images,” in *Proceedings SPIE*,
606 7858 (SPIE, Bellingham, WA, 2010) [78580Y (Nov. 3, 2010)], 7 pp., doi:
607 10.1117/12.870729 (2010).
608 37. S. Andréfouët, M. J. Costello, M. Rast, and S. Sathyendranath, “Preface: Earth
609 observations for marine and coastal biodiversity and ecosystems,” *Remote Sensing of*
610 *Environment*, 112, 3297–3299 (2008).
611 38. C. Dupouy, T. Savranski, J. Lefevre, M. Despinoy, M. Mangeas, R. Fuchs, S. Ouillon, and
612 M. Petit, “Monitoring chlorophyll of the South West Tropical Pacific,” Communication at
613 the 34th International Symposium on Remote Sensing of Environment, Sydney, 10-14
614 April 2011 (2011).
615 39. C. Dupouy, G. Wattelez, R. Fuchs, J. Lefèvre, M. Mangeas, H. Murakami, and R. Frouin,
616 “The colour of the Coral Sea,” *In Proceedings of the 12th International Coral Reef*
617 *Symposium, 18E– The future of the Coral Sea reefs and sea mounts, Cairns, Australia, 9-*
618 13 July 2012, ICRS2012_18E-2 (2012).

40. T. Tadono, M. Shimada, H. Murakami, T. Hashimoto, J. Takaku, A. Mukaida, and S. Kawamoto, “Initial results of calibration and validation for PRISM and AVNIR-2,” *Asian Journal of Geoinformatics,* 6, 4, 11–20 (2006).
41. H. Murakami, T. Tadono, H. Imai, J. Nieke, and M. Shimada, “Improvement of AVNIR-2 radiometric calibration by comparison of cross-calibration and on-board lamp calibration,” *IEEE TGRS, 47, 12, pp. 4051-4059* (2009).
42. F.E. Hoge, and P.E. Lyon, “Satellite retrieval of inherent optical properties by linear matrix inversion of oceanic radiance models: an analysis of model and radiance measurement errors,” *Journal of Geophysical Research,* 101, 16631-16648 (1996).
43. F.E. Hoge, and P.E. Lyon, “Spectral parameters of inherent optical property models: Methods for satellite retrieval by matrix inversion of an oceanic radiance model,” *Applied Optics, 38,* 1657-1662 (1999).
44. P. Lyon, and F. Hoge, “The Linear Matrix Inversion Algorithm,” *Chap. 7 of IOCCG Report Number* **5,** Remote Sensing of Inherent Optical Properties: Fundamentals, Tests of Algorithms, and Applications, Ed. by Z. Lee (2006).
45. Y. Ota, A. Higurashi, T. Nakajima, and T. Yokota, “Matrix formulations of radiative transfer including the polarization effect in a coupled atmosphere-ocean system,” *Journal of Quantitative Spectroscopy and Radiative Transfer,* Vol. 111-6, 878-894 (2010).
46. T. Nakajima, and M. Tanaka, “Matrix formulation for the transfer of solar radiation in a plane-parallel scattering atmosphere,” *J. Quantitative Spectroscopic Radiative Transfer,* 35, 13-21 (1986).

640 47. T. Nakajima, and M. Tanaka, “Algorithms for radiative intensity calculations in
641 moderately thick atmospheres using a truncation approximation,” *Journal of Quantitative*
642 *Spectroscopic Radiative Transfer*, 40, 51-69 (1988).
643 48. K. Stamnes, S.-C. Tsay, W. Wiscombe, and K. Jayaweera, “Numerically stable algorithm
644 for discrete-ordinate-method radiative transfer in multiple scattering and emitting layered
645 media,” *Applied Optics*, 27, 2502-2509 (1988).
646 49. R. Frouin, P-Y. Deschanmps, L. Gross-Colzy, H. Murakami, and T. Y. Nakajima,
647 “Retrieval of Chlorophyll-a Concentration via Linear Combination of ADEOS-II Global
648 Imager Data,” *Journal of Oceanography*, 62, 331-337 (2006).
649 50. R. Zaneveld, A. Barnard, and Z-P. Lee, “Why area Inherent Optical Properties Needed in
650 Ocean-Colour Remote Sensing?,” *Chap. 1 of IOCCG Report Number* 5, Remote Sensing
651 of Inherent Optical Properties: Fundamentals, Tests of Algorithms, and Applications, Ed.
652 by Z. Lee (2006).
653 51. H.R. Gordon, O.B. Brown, R.H. Evans, J.W. Brown, R.C. Smith, K.S. Baker, and D.K.
654 Clark, “A semi-analytic radiance model of ocean color,” *Journal of Geophysical Research*,
655 93 (D9), 10909–10924 (1988).
656 52. Z-P. Lee, K.L. Carder, and R. A. Arnone, “Deriving inherent optical properties from water
657 color: a multiband quasi-analytical algorithm for optically deep waters,” *Applied Optics*,
658 41, 5755-5772 (2002).
659 53. R.M. Pope, and E.S. Fry, “Absorption spectrum (380-700 nm) of pure water. II.
660 Integrating cavity measurements,” *Applied Optics*,36, 8710-8723 (1997).
661 54. L. Kou, D. Labrie, and P. Chylek, “Refractive indices of water and ice in the 0.65-2.5 μm
662 spectral range,” *Applied Optics*, 32, 3531-3540 (1993).

663 55. P.J. Werdell, and S.W. Bailey, “An improved bio-optical data set for ocean color algorithm
664 development and satellite data product validation,” *Remote Sensing of Environment*, 98,
665 122-140 (2005).
666 56. C. Dupouy, J. Neveux, and J.M. Andre, “Spectral absorption coefficient of
667 photosynthetically active pigments in the equatorial Pacific Ocean (165°E–150°W),” *Dee-*
668 *p Sea Research, Part II*, 44, 1881–1906 (1997).
669 57. J. Neveux, and F. Lantoine, “Spectrofluorometric assay of chlorophylls and pheophytins
670 using the least squares approximation technique,” *Deep-Sea Research, Part I*, 40, 1747–
671 1765 (1993).
672 58. A.M. Ciotti, M.R. Lewis, and J.J. Cullen, “Assessment of the relationships between
673 dominant cell size in natural phytoplankton communities and spectral shape of the
674 absorption coefficient,” *Limnology and Oceanography*, 4, 404-417 (2002).
675 59. Z-P. Lee, K.L. Carder, C.D. Mobley, R.G. Steward, and J. S. Patch, “Hyperspectral remote
676 sensing for shallow waters: 2. Deriving bottom depths and water properties by
677 optimization,” *Applied Optics*, 38, 3831-3843 (1999).
678 60. S. Maritorena, A. Morel, and B. Gentili, “Diffise reflectance of oceanic shallow waters:
679 Influence of water depth and bottom albedo,” *Limnol. Oceanogr.*, 39(7), 1689-1703 (1994).
680 61. S. Ouillon, Y. Lucas, and J. Gaggelli, “Hyperspectral detection of sand,” *In, Proc. 7th Int.*
681 *Conf. Remote Sensing for Marine and Coastal Environments, Veridian, Miami, 20-22 May*
682 *2002* (2002).
683 62. S. J. Purkis, and R. Pasterkamp, “Integrating in situ reef-top reflectance spectra with
684 Landsat TM imagery to aid shallow-tropical benthic habitat mapping,” *Coral Reefs*, 23, 5–
685 20 (2004).

686 63. B. A. Franz, “Methods for Assessing the Quality and Consistency of Ocean Color Products,
687 “ http://oceancolor.gsfc.nasa.gov/REPROCESSING/R2009/validation/ (2005).
688 64. Z. P. Lee, A. Weidemann, J. Kindle, R. Arnone, K. L. Carder, and C. Davis, “Euphotic
689 zone depth: Its derivation and implication to ocean-color remote sensing,” *J. Geophys. Res.*
690 112, C03009 (2007).
691 65. Z. P. Lee, “Applying narrowband remote-sensing reflectance models to wideband data”,
692 *Applied Optics*, 48, 3177-3183 (2009).
693 66. R. Frouin, P-Y. Deschamps, and F. Steinmetz, “Environmental effects in ocean color
694 remote sensing,” *Proc. SPIE, Ocean Remote Sensing: Methods and Applications*, Robert J.
695 Frouin, Editors, 745906 Vol. 7459, doi:10.1117/12.829871 (2009).
696 67. G. Thuillier, M. Hersé, D. Labs, T. Foujols, W. Peetermans, D. Gillotay, P.C. Simon, and
697 H. Mandel, “The Solar Spectral Irradiance from 200 to 2400 nm as Measured by the
698 SOLSPEC Spectrometer from the Atlas and Eureca Missions,” *Solar Physics*, 214, 1, 1-22
699 (2003).
700 68. A. Berka, G. P. Anderson, L. S. Bernstein, P. K. Acharya, H. Dothe, M. W. Matthew, S. M.
701 Adler-Golden, J. H. Jr.Chetwynd, S. C. Richtsmeier, B. Pukall, C. L. Allred, L. S. Jeong,
702 and M. L. Hoke, “MODTRAN4 radiative transfer modeling for atmospheric correction,”
703 *Proc. SPIE Vol. 3756, p. 348-353, Optical Spectroscopic Techniques and Instrumentation*
704 *for Atmospheric and Space Research III, Allen M. Larar; Ed.* (1999).
705
706

TABLE LIST

Table 1 Symbols and Definitions

Symbol	*Description*	*Unit*
Chla	chlorophyll-a concentration (sum of chlorophyll-a and divinyl chlorophyll-a)	mg m^{-3}
R_{rs}	remote sensing reflectance above sea surface	sr^{-1}
r_{rs}	remote sensing reflectance just bellow sea surface	sr^{-1}
ρ_t	top of atmosphere reflectance	-
ρ_r	atmospheric molecule reflectance	-
ρ_a	aerosol reflectance, including aerosol-molecule interaction	-
ρ_g	sunglint reflectance	-
ρ_{wc}	whitecap reflectance	-
ρ_w	water-leaving reflectance	-
ρ_{ag}	aerosol + sea surface reflectance ($\equiv \rho_a + \rho_g + \rho_{wc}$)	-
ρ_{agw}	Rayleigh-scattering subtracted reflectance	-
t	atmospheric direct transmittance (sun-surface + surface-satellite)	-
T	direct + diffuse transmittance (sun-surface + surface-satellite)	-
τ_a	aerosol optical thickness	-
M	aerosol model number	-
λ_b	center wavelength of sensor spectral band	nm
α	power function of spectral slope of ρ_{ag}	-
c_{wl}	correction factor of spectral slope	-
pl	air-mass (=2 when satellite and sun are both in nadir)	-
a	total absorption coefficient	m^{-1}
a_w,	absorption coefficient of water	m^{-1}
a_{ph}	absorption coefficient of phytoplankton	m^{-1}
a_d	absorption coefficient of detritus	m^{-1}
a_g	absorption coefficient of CDOM	m^{-1}
a_{pg}	absorption coefficient of particles + CDOM	m^{-1}
a_{ph}'	model spectrum of phytoplankton absorption normalized at 442 nm	-
a_{dg0}	detritus+CDOM absorption at 442 nm	m^{-1}
S	spectral slope of a_{dg}'	-
a_{dg}'	model spectrum of detritus+CDOM absorption normalized at 442 nm	-
r_{pg}	ratio of a_{ph} and a_{dg} at 442 nm	-
a_{pg0}	phytoplankton+detritus+CDOM absorption at 442 nm	m^{-1}
a_{pg}'	model spectrum of phytoplankton+detritus+CDOM absorption normalized at 442 nm	-
b_b	total backscattering coefficient	m^{-1}
b_w	scattering coefficient of water	m^{-1}
b_{bw}	backscattering coefficient of water	m^{-1}
b_{bp}	backscattering coefficient of particles	m^{-1}
b_{bp0}	particle backscattering at 442 nm	m^{-1}
Y	spectral exponent of b_{bp}'	-
b_{bp}'	model spectrum of particle backscattering normalized at 442 nm	-
ρ_b	albedo of sea floor	-
H	bottom depth	m
r_{rs}^{dp}	remote-sensing reflectance for optically deep water	sr^{-1}
θ_{0w}	subsurface solar zenith angle from nadir	radian
θ_w	subsurface viewing angle from nadir	radian
θ_a	above-surface viewing angle from nadir	radian
κ	attenuation coefficient	m^{-1}
D_u^C	optical path-elongation factors for scattered photons from the water column	-
D_u^B	optical path-elongation factors for scattered photons from the bottom	-
L_{wn}	normalized water-leaving radiance	mW /μm/sr

708

709

Table 2 AVNIR-2 bands, cross-cal coefficients, and gas abruption coefficients

AVNIR-2 band number (b)	1	2	3	4
Center wavelength (λ_b) [nm]	463.0	560.0	652.1	820.6
Solar irradiance at 1 AU (F_0) [W/m^2 /μm]	1943.3	1813.7	1562.3	1076.5
Calibration correction coefficients (f_{vc})	0.976	1.019	1.001	0.958
Ozone absorption coefficient (k_{oz})	1.314×10^{-5}	1.191×10^{-4}	8.697×10^{-5}	5.461×10^{-6}
Water vapor k_{wv}	0	1.763×10^{-4}	2.595×10^{-4}	1.223×10^{-3}
absorption coefficient k_{wv2}	0	0	0	-2.580×10^{-6}
O_2 absorption coefficient (k_{O2})	0	0	0	1.352×10^{-4}

710

711

Table 3 Spectra of a_w, b_{bw}, and a_{ph}

Central wavelength (nm)	Band 1 (463.0)	Band 2 (560.0)	Band 3 (652.1)	Band 4 (820.6)	Band A (442)	Band B (555)
a_w [53]	0.01085	0.07935	0.37969	3.41656	0.00684	0.05969
b_{bw} [54]	0.00208	0.00091	0.00048	0.00018	0.00246	0.00093
(i) *New Caledonia* a_{ph}	0.84224	0.19490	0.11668	0.0	1.0	0.19869
(ii) *Picoplankton* a_{ph} [58]	0.80046	0.07025	0.11225	0.0	1.0	0.04378
(iii) *Microplankton* a_{ph} [58]	0.89368	0.37280	0.37919	0.0	1.0	0.37556

712 The values for bands 1-4 are weighted by the spectral response of the AVNIR-2 bands. The
713 a_{ph} spectra (i) is used in (A) and (D)-(F) of Table 4, (ii) and (iii) are used in (B) and (C) of
714 Table 4 respectively. Bands A and B (at 442 nm and 555 nm, respectively) were obtained
715 by weighting using a rectangular response with ±5 nm width.

716

717

718

719

Table 4 Comparison between in situ and AVNIR-2 IOP estimates using different sets of IOP spectra

Test No.		a_{ph} spectrum	*S*	*Y*	AVNIR-2 a_{pg} vs. in situ a_p at 442 nm×1.52			AVNIR2 vs. in situ b_{bp} at 555 nm		
					r	*bias*	*RMSD*	*r*	*bias*	*RMSD*
without bottom	(A)	*New Caledonia*	-0.010	-1.4	0.91	0.188	0.489	0.94	0.023	0.042
	(B)	***Picoplankton*** [58]	-0.010	-1.4	0.94	0.062	0.124^{-}	0.91	0.010	0.012^{-}
	(C)	***Microplankton*** [58]	-0.010	-1.4	0.93	0.466	1.134^{+}	0.91	0.056	0.119^{+}
	(D)	*New Caledonia*	**-0.018**	-1.4	0.94	0.090	0.191^{-}	0.93	0.012	0.015^{-}
	(E)	*New Caledonia*	-0.010	**-0.0**	0.94	0.033	0.098^{-}	0.93	0.012	0.015^{-}
	(F)	*New Caledonia*	-0.010	**-2.0**	0.91	0.340	0.909^{+}	0.93	0.034	0.076^{+}
with bottom	(A)	*New Caledonia*	-0.010	-1.4	0.95	0.118	0.290	0.96	0.015	0.025
	(B)	***Picoplankton*** [58]	-0.010	-1.4	0.80	-0.011	0.087^{-}	0.55	0.002	0.010^{-}
	(C)	***Microplankton*** [58]	-0.010	-1.4	0.93	0.458^{+}	1.132^{+}	0.91	0.055	0.118^{+}
	(D)	*New Caledonia*	**-0.018**	-1.4	0.91	0.016	0.059^{-}	0.75	0.005	0.009^{-}
	(E)	*New Caledonia*	-0.010	**-0.0**	0.72	-0.020	0.098^{-}	0.49	0.004	0.012^{-}
	(F)	*New Caledonia*	-0.010	**-2.0**	0.91	0.315	0.898^{+}	0.93	0.031	0.074^{+}

Sample number N=15. In situ averages of $a_p \times 1.52$ at 442 nm and b_{bp} at 555 nm were 0.099 m^{-1} and 0.0055 m^{-1}, respectively. Superscripts $^{-}$ and $^{+}$ show values that were smaller and larger compared to case (A) at significance level of 95%. *S* and *Y* are defined in the text (Eqs. (12) and (13)).

726

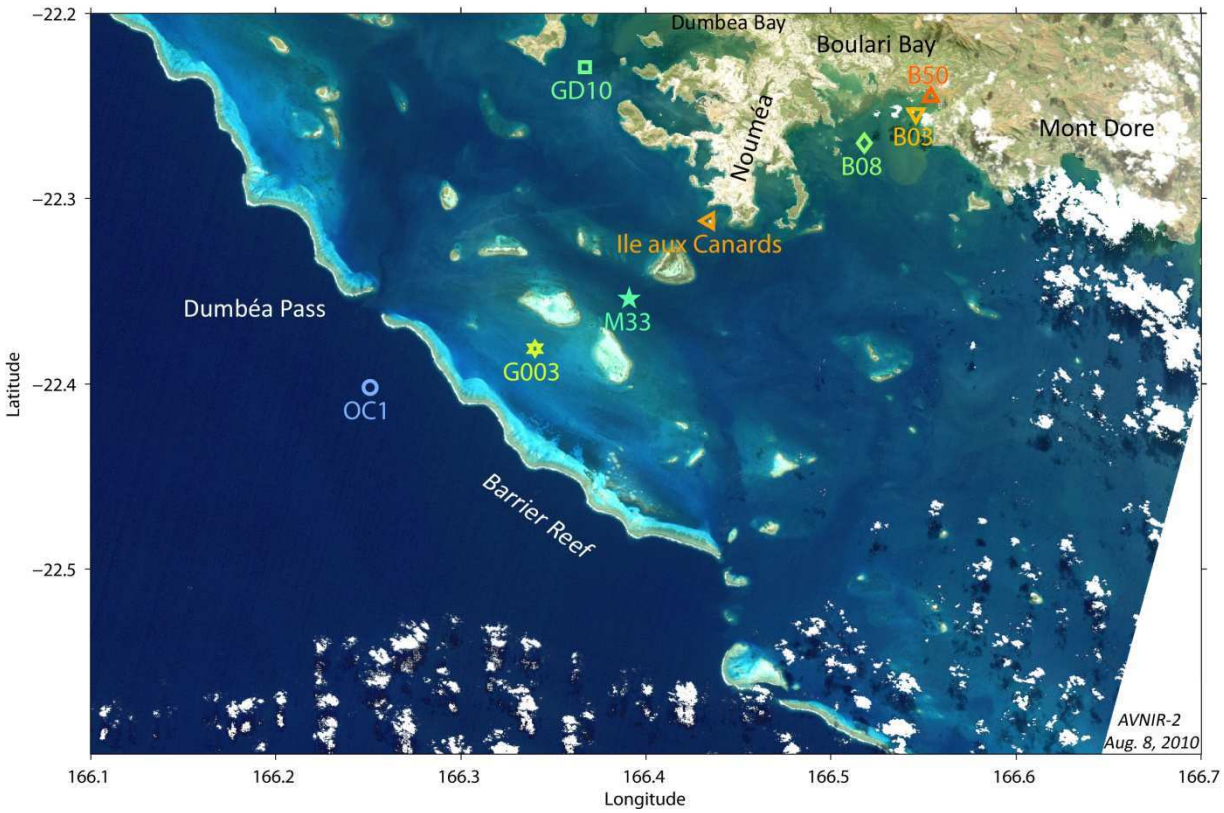

727

728

729 Figure 1 New Caledonia lagoon and in situ observation stations used in this study (B50, B03,

730 B08, GD10, Ile aux Canards, M33, G003, and OC1). The background image is the RGB image

731 of R_{rs} at 652 nm, 560 nm, and 463 nm derived from this study.

732

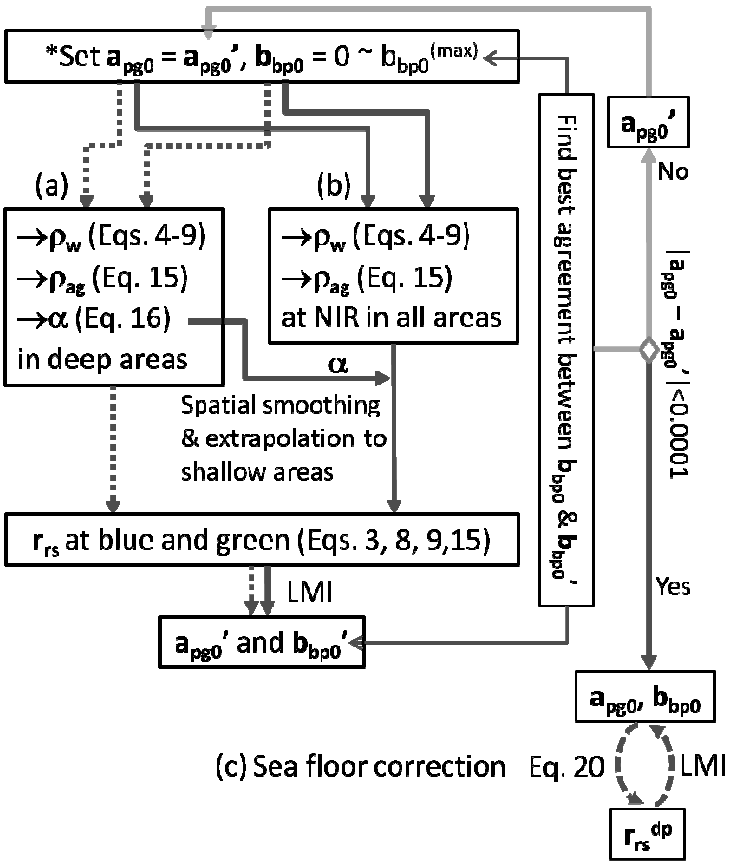

Figure 2 Processing flow of the IOP and aerosol correction. The operation starts from *. The first flow (a) produces the α, which is used in the second flow (b). After a_{pg0} is converted ($|a_{pg0}) - a_{pg0}'| < 0.0001$), the sea-floor correction (c) is applied..

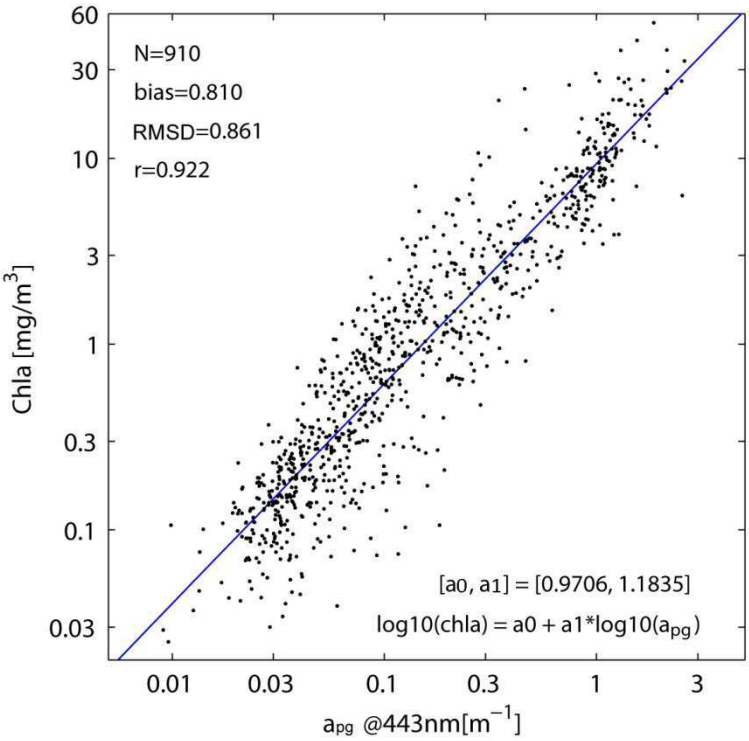

Figure 3 Relation between *Chla* and a_{pg} or blue-green R_{rs} ratio ($\log_{10}$ base) based on NOMAD [55]. N, RMSD, and r indicate sample number, root mean square error of the regression ($\log_{10}$ scale), and the correlation. a0 and a1 are coefficients of the linear regression, *i.e.*, $\log_{10}(Chla) = 0.9706 + 1.1835 \log_{10}(a_{pg})$.

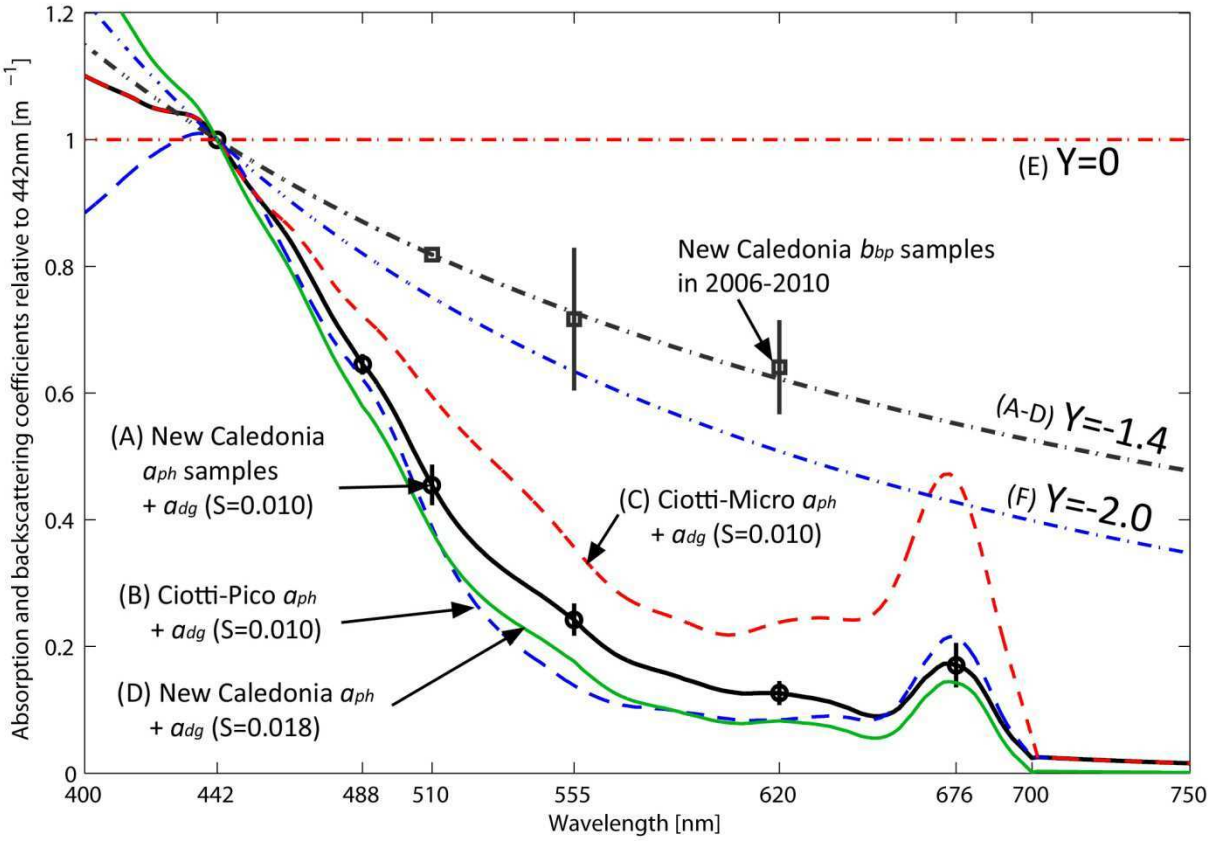

Figure 4 Model spectra of a_{pg} and b_{bp} used in this study. Models of a_{pg} (A) and b_{bp} (Y=−1.4) were set from the New Caledonia measurements. S was defined as $a_{dg}=\exp(S\times(\lambda-442))$ as in Eq. (12), and Y was defined as $b_{bp}=(\lambda/442)^{Y}$ in Eq. (13). The spectra for picoplankton (B) and microplankton (C) from [58] were used for comparison. Curves are indicated for different Y slopes for b_{bp} (Y=0 and Y=−2, see also Table 4). Bars show standard deviation of the in situ measurements.

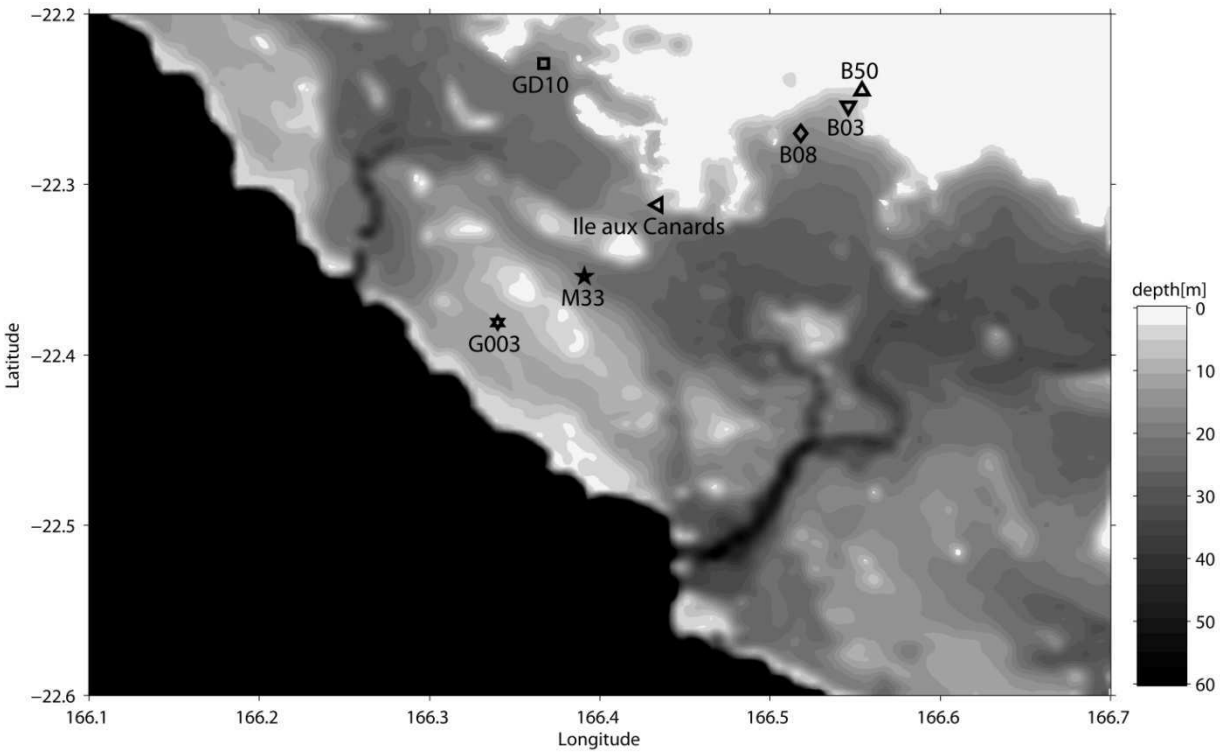

Figure 5 Bathymetry in the target area [12]. Deep areas (>60m) are filled by black.

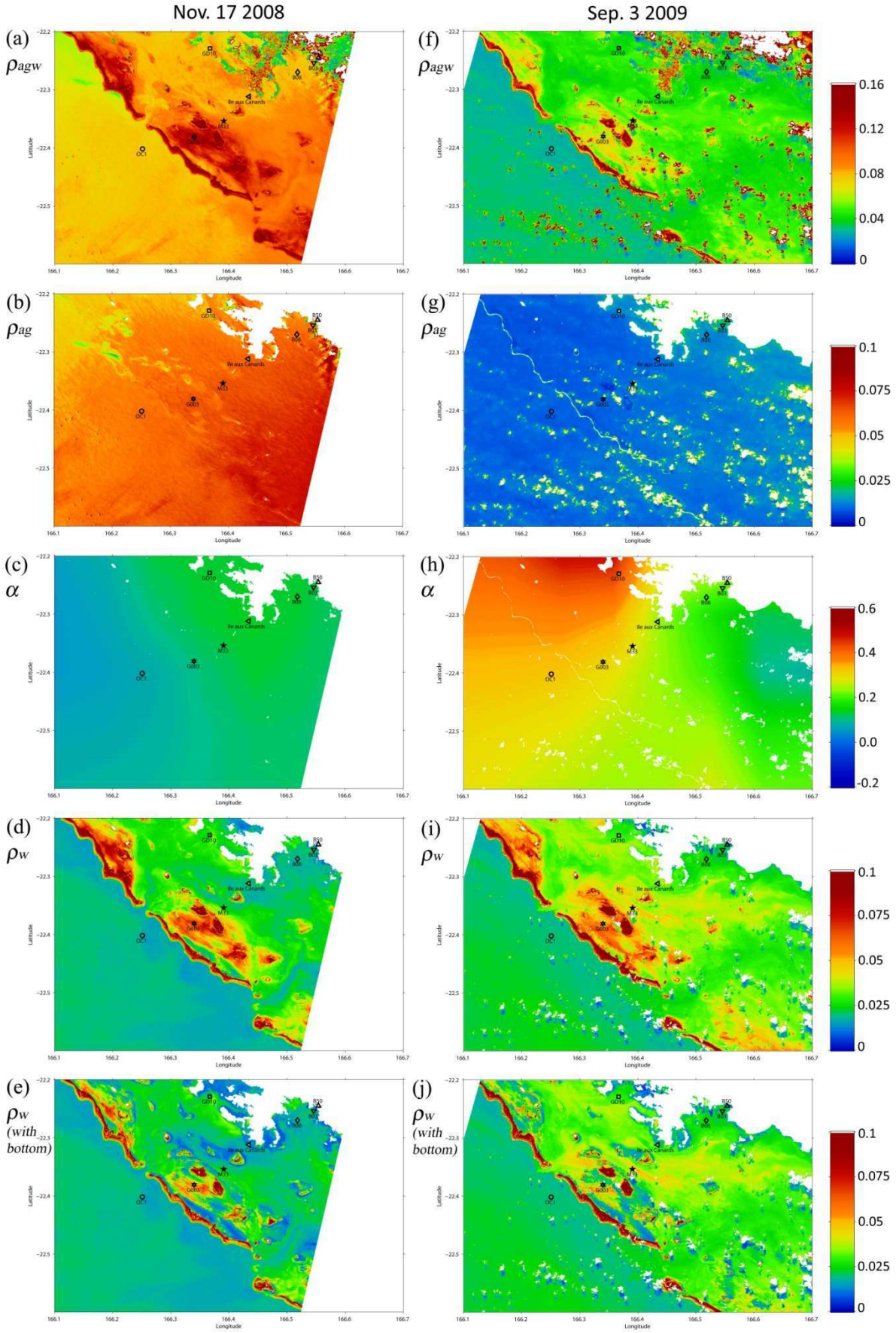
Nov. 17 2008
Sep. 3 2009
(a) ρ_{agw}
(b) ρ_{ag}
(c) α
(d) ρ_w
(e) ρ_w (with bottom)
(f) ρ_{agw}
(g) ρ_{ag}
(h) α
(i) ρ_w
(j) ρ_w (with bottom)
Latitude
Longitude
Ile aux Canards
0.16
0.12
0.08
0.04
0
0.1
0.075
0.05
0.025
0.6
0.4
0.2
0.0
-0.2

760

761 Figure 6 Examples of AVNIR-2-derived ρ_{agw}, ρ_{ag}, α, ρ_w without bottom correction, and ρ_w at
762 463 nm with bottom correction for 17 Nov 2008 (a-e) and for 3 Sep. 2009 (f-j) (using model
763 (A) in Table 4). The field measurement sites are shown in each panel.

764

765

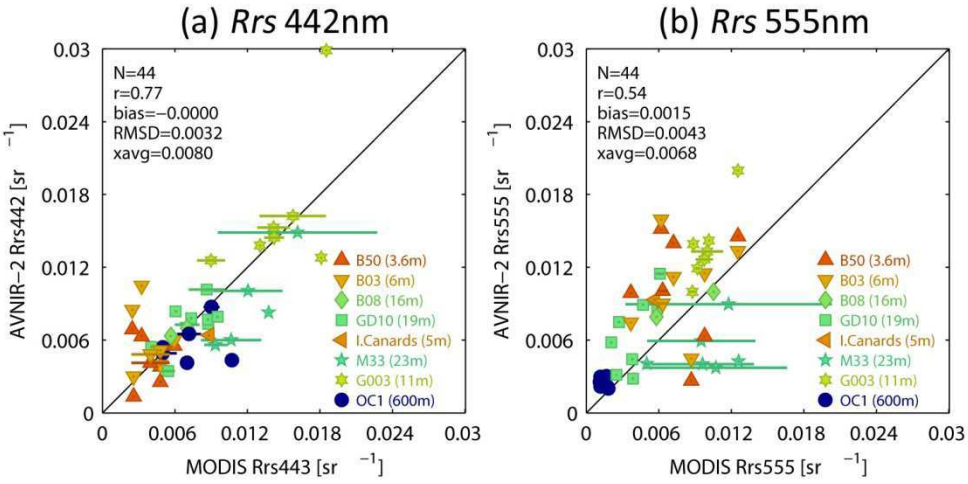

766

767

768 Figure 7 Comparison between AVNIR-2 *Rrs* at 442 nm and MODIS *Rrs* at 443 nm (a) and at

769 555 nm (b) for 44 samples. The markers distinguish between the different observation stations.

770 The horizontal bars show the standard deviation of the multiple MODIS scenes.

771

772

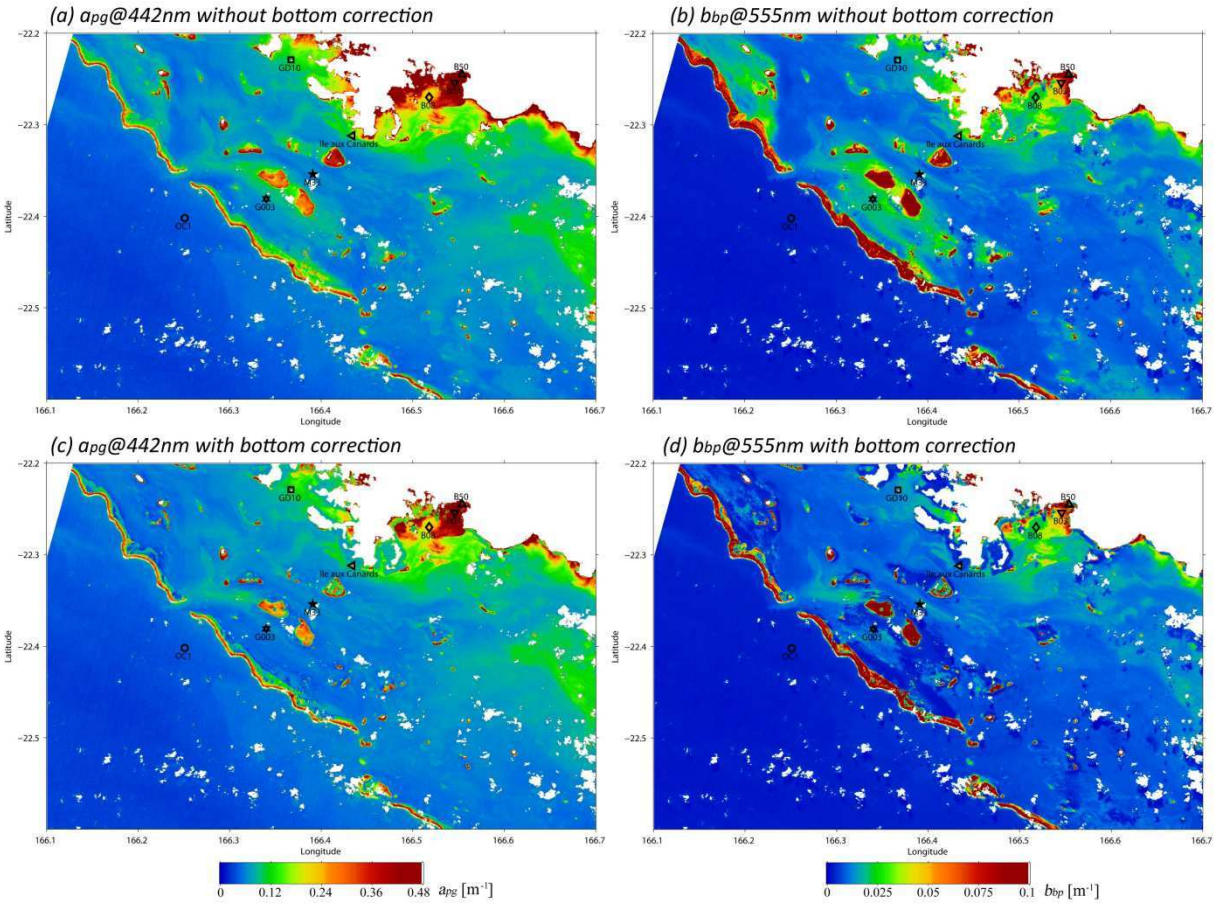

Figure 8 AVNIR-2 estimation of (a) a_{pg} at 442nm and (b) b_{bp} at 555nm on 3 Sep 2009 (using model spectra (A) in Table 4 and no correction of the bottom reflection). (c) and (d) are same as (a) and (b) except applying the correction of the bottom reflection. Markers show in situ observation stations.

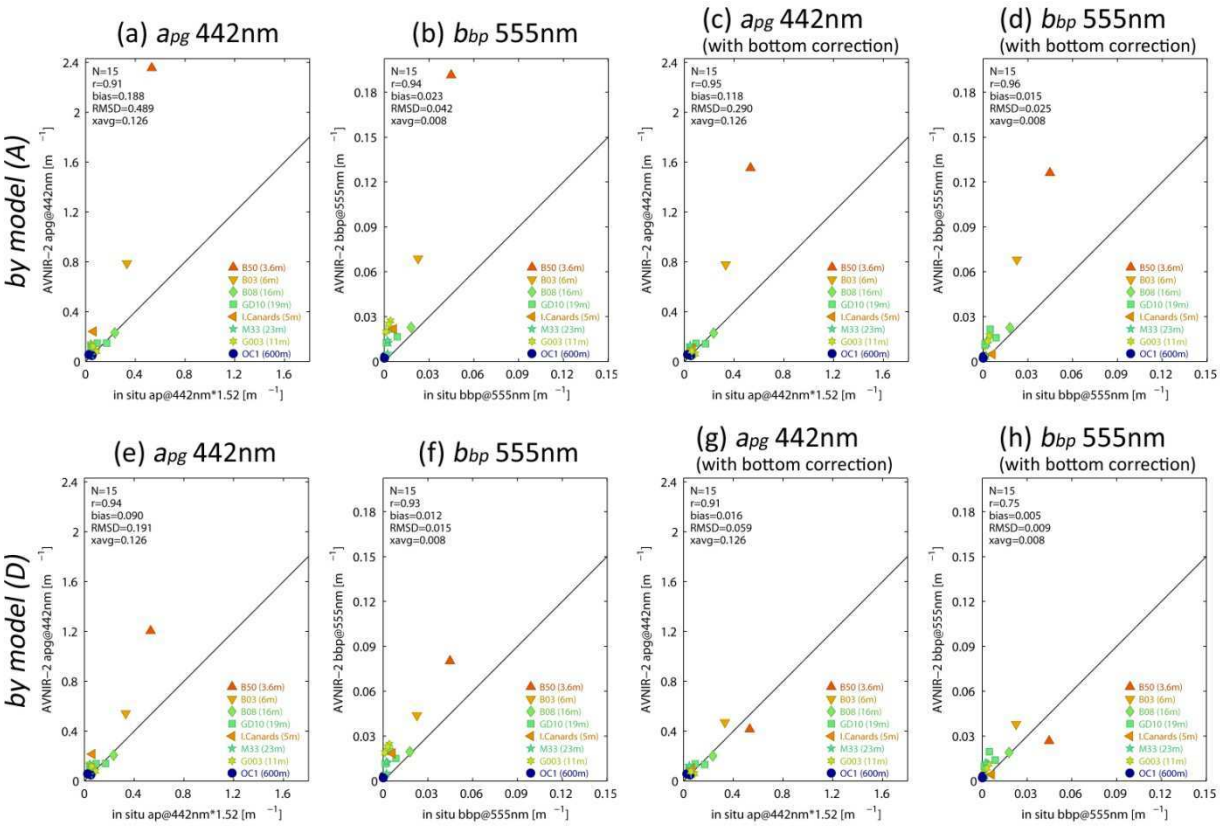

Figure 9 Scatter diagrams of (a) AVNIR-2 a_{pg} and in situ a_p (×1.52) at 442 nm, (b) b_{bp} at 555 nm from model (A) in Table 4. (c) and (d) are same as (a) and (b) except applying the correction of the bottom reflection. N, r, bias, and RMSD, indicate sample number, correlation coefficient, bias of AVNIR-2 from in situ, and root mean square difference. xavg indicates the average of in situ data (in m^{-1}). (e)-(h) are same as (a)-(d) except they are derived from model (D).

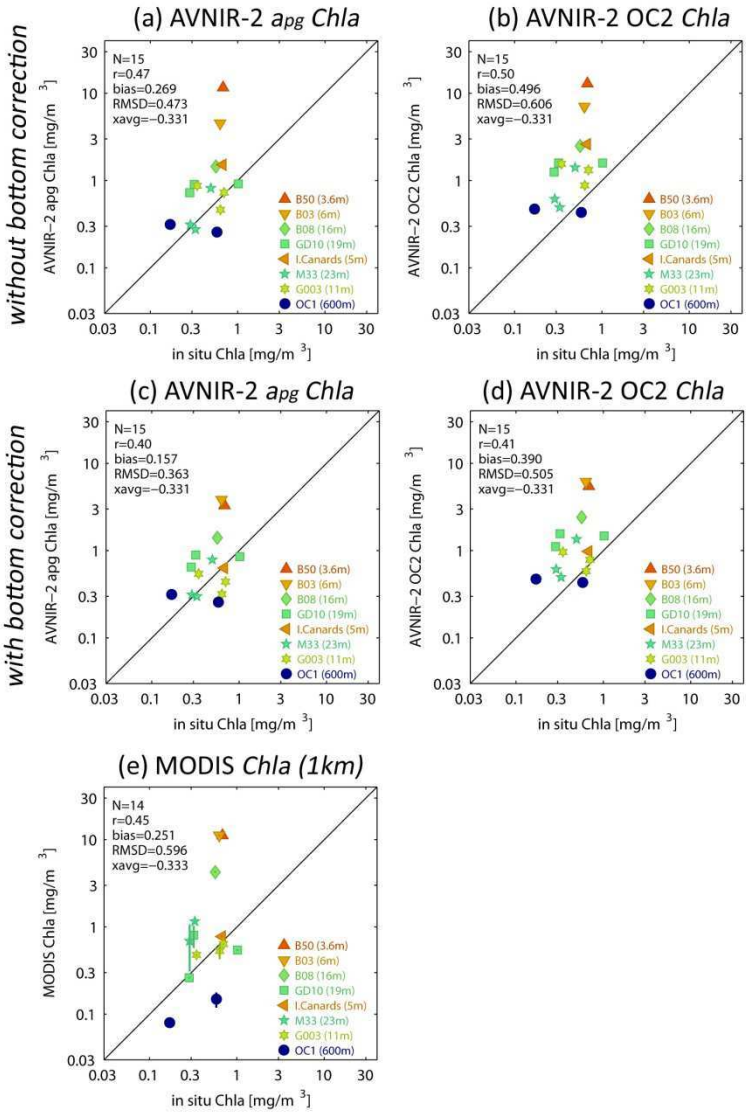

Figure 10 Scatter diagrams of in situ *Chla* and (a) *Chla* from AVNIR-2 a_{pg}, (b) *Chla* from AVNIR-2 OC2M-HI, (c) and (d) are same as (a) and (b) except applying the bottom correction, (e) *Chla* from the MODIS standard OC3M (1 km), and (f) the scatter plot between AVNIR-2 a_{pg} *Chla* and the MODIS OC3M *Chla*. Bars show the standard deviation of the multiple MODIS scenes around the AVNIR-2 observation dates or the standard deviation of 3×3 pixels of AVNIR-2 data. N, r, bias, RMSD, and xvag show sample number, correlation coefficient, bias, root mean square difference, and the average of x-axis variables in $\log_{10}$ scale.

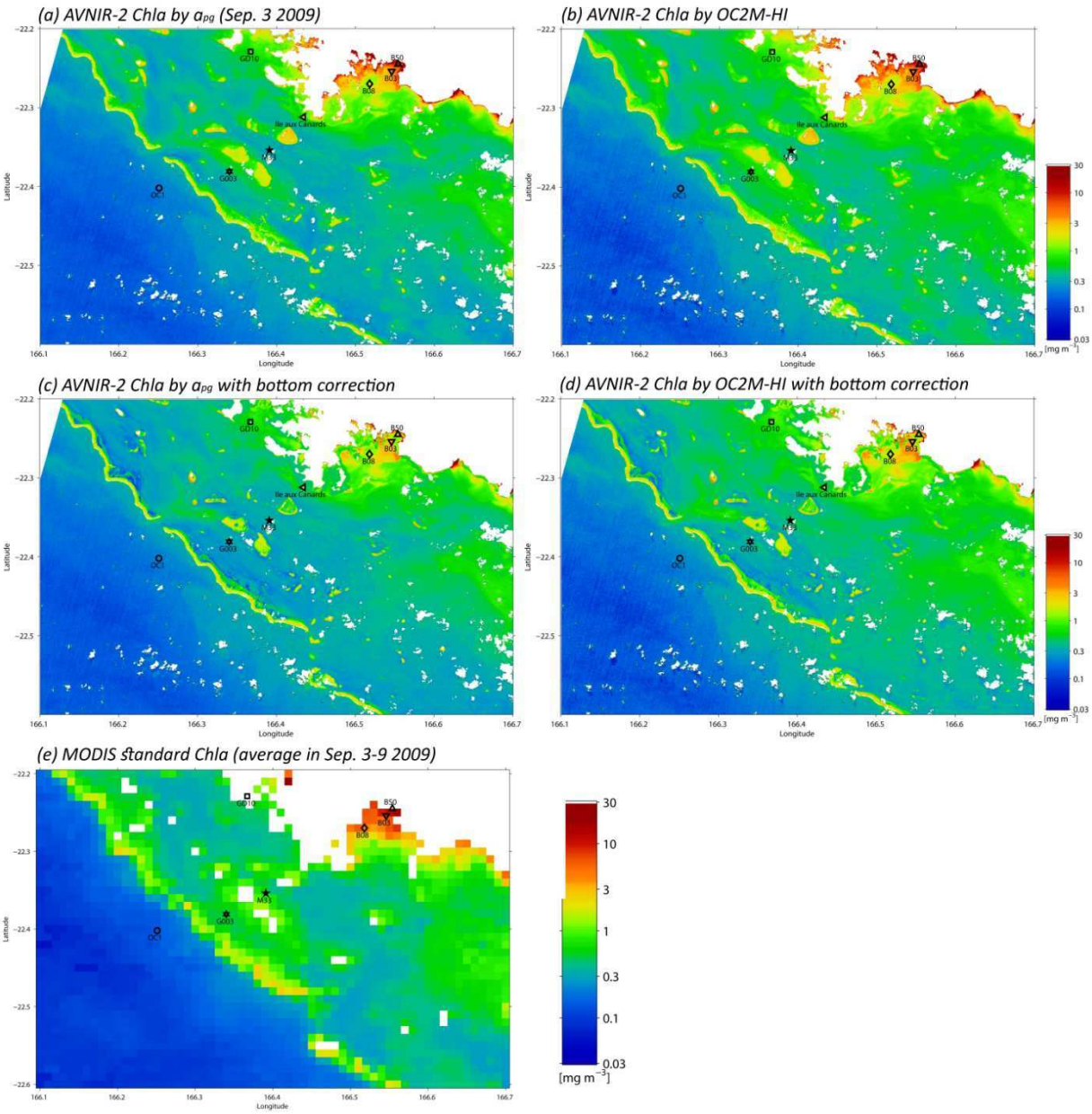

801

802 Figure 11 (a), (b), and (e) are *Chla* from a_{pg}, *Chla* from OC2M-HI (Sep. 3 2009) and the
803 MODIS standard *Chla* (average from Sep. 3 to Sep. 9 in 2009). (c) and (d) are the same as (a)
804 and (b) except applying the bottom correction. Markers show the in situ observation stations on
805 Sep 9 2009.